



Fachlicher Schlussbericht des BMBF Forschungsvorhabens
„Verbundprojekt: Grundlegende Untersuchungen zur Immobilisierung
langlebiger Radionuklide mittels Einbau in endlagerrelevante Keramiken
(Conditioning)“

Teilprojekt B

Das diesem Bericht zugrundeliegende Vorhaben wurde mit Mitteln des Bundesministeriums für Bildung und Forschung unter dem Förderkennzeichen 02NUK021B gefördert.

Die Verantwortung für den Inhalt dieser Veröffentlichung liegt bei den Autoren.

Andreas C. Scheinost (Projektleiter)

Janeth Marisol Lozano Rodriguez

Institut für Ressourcenökologie

Forschungszentrum Dresden Rossendorf (HZDR)

Bautzener Landstr. 400, 01328 Dresden

Inhalt

1	Kurzbeschreibung.....	4
1.1	Aufgabenstellung.....	4
1.2	Voraussetzungen unter denen das Vorhaben durchgeführt wurde	4
1.3	Planung und Ablauf des Vorhabens	4
1.4	Stand von Wissenschaft und Technik, an den angeknüpft wurde	5
1.5	Zusammenarbeit mit anderen Stellen.....	6
2	Darstellung der Ergebnisse.....	8
2.1	Erzieltes Ergebnis.....	8
2.1.1	Structure of lanthanide phosphates.....	8
2.1.2	The local structure of Pu in La/Pu monazite solid solutions	9
2.1.3	The local structure of La and Eu in La/Eu monazite solid solutions	16
2.1.4	The local structure of Cm in Cm ³⁺ -doped La _{1-x} Gd _x PO ₄ monazite.....	21
2.1.5	Incorporation of thorium in thorite-xenotime solid solutions	23
2.1.6	The local structure of Sm and Tb in Sm _{1-x} Tb _x PO ₄ : Monazite to xenotime transition	28
2.1.7	The local structure of La/Eu/Lu phosphate: Monazite to xenotime transition.....	30
2.1.8	Rhabdophane	34
2.1.9	The local structure of iodate in layered double hydroxides.....	36
2.2	Conclusions.....	38
2.2.1	Relevance of results with respect to ceramic waste forms.....	38
2.2.2	Knowledge gaps and outlook for future research.....	39
2.2.3	References.....	40
2.3	Fortschritt auf dem Gebiet des Vorhabens anderer Stellen	43
2.4	Publikationen der Ergebnisse	44
2.4.1	Begutachtete Artikel in wissenschaftlichen Zeitschriften	44
2.4.2	Vorträge auf nationalen und internationalen Konferenzen.....	45
2.4.3	Poster auf nationalen und internationalen Konferenzen.....	45

1 Kurzbeschreibung

1.1 Aufgabenstellung

Die sichere Entsorgung radioaktiver Abfälle ist eine dringende wissenschaftliche und gesellschaftliche Aufgabe von nationalem und internationalem Interesse, die in den nächsten Jahrzehnten bewältigt werden muss. Die zum Teil hochradioaktiven Abfälle sollen in ein tiefengeologisches Endlager eingebracht werden, wobei die Sicherheit für Zeiträume von einer Million Jahren gewährleistet werden muss.

Keramische Materialien werden seit Jahrzehnten aufgrund ihrer physikalischen und chemischen Eigenschaften als erfolgversprechende Alternative zu Borosilikatgläsern als Matrix für die Immobilisierung und Endlagerung radioaktiver Abfälle diskutiert [Lutze1988, Donald1997, Lumpkin2006, Weber2009]. Allerdings konnten bis heute die hochkomplexen Zusammenhänge zwischen Struktur und Stabilität bezüglich des Langzeitverhaltens keramischer Abfallformen unter endlagerrelevanten Bedingungen nicht ausreichend beschrieben werden.

Im Rahmen dieses Vorhabens sollten experimentelle Untersuchungen mit komplementär durchgeführten Modellrechnungen verknüpft werden, um auf der Grundlage von Struktur-/Eigenschaftsbeziehungen ein tieferes grundlegendes Verständnis zu entwickeln, mit dem sich die Prozesse im Endlager auf molekularer Ebene beschreiben und belastbare Aussagen bezüglich der Langzeitstabilität von keramischen Abfallmatrizes und ihres Rückhaltevermögens für Radionuklide (insb. Actiniden) unter Endlagerbedingungen treffen lassen.

1.2 Voraussetzungen unter denen das Vorhaben durchgeführt wurde

Um das Forschungsvorhaben zur Immobilisierung langlebiger Radionuklide in keramischen Materialien realisieren zu können, mussten Kompetenz und Expertise auf den Gebieten Analytik, Materialwissenschaften und Modellierung sowie Radiochemie kombiniert werden. Darüber hinaus musste für den sicheren Umgang mit radioaktiven Stoffen die erforderliche Infrastruktur, z.B. radioaktive Kontrollbereiche und Handschuhboxen sowie die notwendigen Sicherheitsvorkehrungen und entsprechenden Erfahrungen bereitgestellt werden. Durch die Bildung eines Verbundes aus Instituten der HGF-Forschungszentren in Dresden-Rossendorf und Jülich sowie der Universitäten in Aachen, Hannover und Frankfurt wurden aufgrund deren komplementärer Expertise sowie der vorhandenen Umgangsgenehmigungen mit radioaktiven Materialien ideale Voraussetzungen geschaffen, um die Vorhabensziele zu erreichen.

1.3 Planung und Ablauf des Vorhabens

Zur Beschreibung der Langzeitstabilität keramischer Abfallformen in einem Endlager ist ein fundiertes Verständnis der Mechanismen der Radionuklidimmobilisierung sowie der hoch-komplexen Prozesse der Auflösung der Abfallmatrix und der damit verbundenen Radionuklidfreisetzung unter Endlagerbedingungen auf molekularer Ebene notwendig. Dieses mechanistische Prozessverständnis sollte durch die gezielte Untersuchung ausgewählter Materialien mit einer Kombination von modernen experimentellen und theoretischen Methoden gewonnen werden. Für die Durchführung des Vorhabens wurden die folgenden, eng miteinander verzahnten Arbeitspakete definiert:

- AP1: Synthese der Immobilisierungsmatrizes
- AP2: Strukturelle Charakterisierung
- AP3: Strahlenschäden
- AP4: Thermodynamik und physikalische Eigenschaften
- AP5: Korrosionsbeständigkeit unter Endlagerbedingungen
- AP6: Publikationen

Im Rahmen der Vorhabensdurchführung wurden die Forschungsaktivitäten und komplementären Expertisen von sieben Partnern in einem Konsortium gebündelt, um einen Beitrag zur Erweiterung des derzeitigen Wissenstandes sowie auch zur Aufrechterhaltung und Weiterentwicklung des

Kenntnisstandes (Kompetenzerhalt und Nachwuchsförderung) auf dem Gebiet der Entsorgung radioaktiver Abfälle zu leisten.

Die dazu erforderlichen Forschungsaktivitäten wurden durch einen intensiven Informationsaustausch im Rahmen der halbjährlich organisierten Projekttreffen abgestimmt und in enger Vernetzung der Projektpartner entsprechend ihrer individuellen Kernkompetenzen durchgeführt. Die Vorhabensergebnisse wurden in Publikationen in Fachzeitschriften und durch Beiträge auf Konferenzen dem nationalen und internationalen Fachpublikum präsentiert. Darüber wurden im Rahmen des Vorhabens eine internationale Sommerschule „8th European Summer School on Separation Chemistry and Conditioning as well as Supramolecular, Intermolecular, Interaggregate Interactions“ (Bonn/Bad Godesberg, Juli 2014) sowie eine spezifische Session beim MRS-Symposium „Scientific Basis for Nuclear Waste Management XXXIX“ (Montpellier, November 2015) organisiert, um den Nachwuchswissenschaftlern eine Plattform zur Präsentation ihrer Projektergebnisse zu geben und Kontakte auf internationaler Ebene zu knüpfen.

Das Verbundprojekt „Grundlegende Untersuchungen zur Immobilisierung langlebiger Radionuklide mittels Einbau in endlagerrelevante Keramiken (Conditioning)“ (Förderkennzeichen O2NUK021A bis G) wurde vom Bundesministerium für Bildung und Forschung (BMBF) für eine Laufzeit von 3 Jahren (01.10.2012 – 30.09.2015) bewilligt. Aus verschiedenen organisatorischen und technischen Gründen (z.B. zeitaufwändige Akquise geeigneter Nachwuchswissenschaftler; Abschaltung externer Einrichtungen zur Durchführung von Bestrahlungsexperimenten (AP 3 (Strahlenschäden), sowie Verzögerungen bei Radioaktivtransporten) erfolgte eine kostenneutrale Verlängerung des Projektes für alle Verbundpartner bis zum 31. März 2016 und für die Teilprojekte (O2NUK021A-C) bis zum 30. Juni 2016.

1.4 Stand von Wissenschaft und Technik, an den angeknüpft wurde

Die Entwicklung eines zuverlässigen Entsorgungskonzeptes zur sicheren Endlagerung radioaktiver Abfälle und die damit verbundenen wissenschaftlichen Fragestellungen bleiben sowohl für Länder, die die nachhaltige Nutzung der Kernenergie fortführen als auch für Länder, die den Ausstieg aus der Kernenergie beschlossen haben, wie z.B. Deutschland eine technische, politische und wirtschaftliche Notwendigkeit und Herausforderung.

Die Immobilisierung hochradioaktiver Abfälle in keramischen Materialien als Alternative zur Verglasung ist in den letzten 40 Jahren international intensiv erforscht worden [Lutze1988, Donald1997, Lumpkin2006, Weber2009], während dieser Forschungszweig auf nationaler Ebene seit ungefähr 25 Jahren völlig vernachlässigt wurde. Dennoch existieren hinsichtlich der Konditionierung von Plutonium, den langlebigen Actiniden (²⁴³Am, ²⁴⁷Cm, ²³⁷Np) und den langlebigen Spaltprodukten wie z.B. ⁹⁹Tc, ¹²⁹I nur wenige Forschungsergebnisse.

Keramiken erweisen sich aufgrund ihres höheren Aufnahmevermögens für bestimmte Radionuklide als vorteilhafte Abfallformen für spezifische Abfallströme, zumal die Natur etliche mineralische „Vorbilder“ (natürliche Analoge) für langzeitstabile, keramische Abfallformen zur Verfügung stellt. Mit der Entwicklung neuer Entsorgungsstrategien für Plutonium aus der Abrüstung nuklearer Waffensysteme sind erstmalig einphasige maßgeschneiderte Keramiken als Endlagerungsmatrizes, z.B. Phosphate mit Monazitstruktur [Boatner1988, Oelkers2008] und Zirconate mit Pyrochlorstruktur [Ewing2004, Weber1998] in Betracht gezogen worden. Es hat sich gezeigt, dass einphasige Keramiken als langzeitstabile Endlagerungsmatrizes in Frage kommen und neue Perspektiven bezüglich der sicheren Endlagerung von hochradioaktiven Abfällen bieten.

Zur Entwicklung eines belastbaren Entsorgungskonzeptes für keramische Abfallformen ist eine genaue thermodynamische Beschreibung der keramischen Abfallform notwendig. Dazu gehören die strukturelle Aufklärung der Einbaumechanismen der Radionuklide in die Matrizes während der Immobilisierung sowie der Phasenstabilität von Mischkristallsystemen. Darüber hinaus sind Einflüsse von Syntheseverfahren und Sinterprozessen auf die Mikrostruktur und die physikalischen Eigenschaften der Matrizes zu berücksichtigen.

Hinsichtlich der chemischen Stabilität werden in der Literatur Korrosionsversuche unter statischen und dynamischen Bedingungen beschrieben. Der Temperaturbereich kann sich von Raumtemperatur bis

200°C und über Zeiträume von ein paar Tagen bis hin zu mehreren Jahren für die Erfassung der Daten erstrecken [Oelkers2002]. Es resultieren Datensätze, die die Auslaugrate in Abhängigkeit von der Temperatur oder dem pH-Wert widerspiegeln, aus denen deutlich hervorgeht, dass keramische Wirtsphasen chemisch beständiger sind als die Borosilikatgläser. Die Versuchsbedingungen dieser Tests zur Bestimmung der Auslaugraten variieren zum Teil sehr stark, was einen direkten Vergleich der Ergebnisse oftmals sehr schwierig erscheinen lässt.

Die Strahlenschäden in keramischen Abfallformen sind bereits vielfältig untersucht worden [Ewing1995, Weber1998, Ewing2004]. Einphasige Keramiken durchlaufen dabei meist Phasentransformationen vom kristallinen in einen amorphen Zustand. Die Amorphisierung geht einher mit einer Veränderung der Mikrostruktur durch Volumenexpansion (5 bis 20%) [Weber1998, Chartier2001] bzw. –kontraktion [Belin2009, Martin2009] und Rissbildungen in der Keramik, wodurch die möglichen Kontakt- bzw. Grenzflächen für eindringende Lösungen vergrößert und die Löslichkeit erhöht wird. Die Rolle des α -Rückstoßeffectes bei diesen Prozessen wurde bei bisherigen Forschungen jedoch vernachlässigt und sogar unterschätzt [Ewing2011]. Die geplanten Arbeiten in diesem Projekt sollen zur Aufklärung der Mechanismen der reversiblen Phasentransformation kristallin \leftrightarrow amorph beitragen. Diese Fragestellung ist in der Literatur trotz jahrzehntelanger Forschung bislang nicht hinreichend beantwortet worden.

Insofern wurden die beobachteten Effekte in der Literatur meist phänomenologisch beschrieben. Systematische mechanistische Betrachtungen zusammen mit komplementären Modellrechnungen hingegen waren rar und bedurften der weiteren intensiven Forschungsentwicklung.

1.5 Zusammenarbeit mit anderen Stellen

Der Verbund setzt sich aus sieben nationalen Partnern zusammen, welche die für eine zielgerichtete und erfolgreiche Durchführung des Vorhabens entsprechende Expertise, Spezialisierung und langjähriger Erfahrung besitzen:

- Forschungszentrum Jülich GmbH, Institut für Energie und Klimaforschung – IEK-6: Nukleare Entsorgung und Reaktorsicherheit (FZJ-IEK6; 02NUK021A)
- Helmholtz-Zentrum Dresden-Rossendorf, Institut für Ressourcenökologie (HZDR-IRO; 02NUK021B & 02NUK021C)
- RWTH Aachen University – Institut für Gesteinshüttenkunde (RWTH-GHI; 02NUK021D)
- RWTH Aachen University – Institut für Kristallografie (RWTH-IFK; 02NUK021E)
- Johann-Wolfgang-Goethe-Universität Frankfurt – Institut für Geowissenschaften (GUF-IFG; 02NUK021F)
- Leibniz Universität Hannover – Institut für Radioökologie und Strahlenschutz (LUH-IRS; 02NUK021G).
- Brenk Systemplanung GmbH (BS), Aachen: Die BS handelte im Unterauftrag des FZJ-IEK6.

Das Konsortium verfügte bereits zu Beginn des Projektes über intensive Kontakte zu und Kooperationen mit international anerkannten Forschungsgruppen auf dem Gebiet nuklearer Abfallformen und der Festkörperchemie/-physik, die im Rahmen des Projektes gepflegt und weiter ausgebaut wurden. Diese Forschungsinstitutionen wurden insbesondere aufgrund ihrer exzellenten Expertise und Reputation ausgewählt:

Das FZJ-IEK6 kooperierte auf dem Gebiet der nuklearen Entsorgungsforschung bereits unter anderem mit dem Institut de Chimie Séparative de Marcoule (ICSM), Marcoule, Frankreich; dem Immobilisation Science Laboratory, University of Sheffield, Großbritannien; Australian Nuclear Science and Technology Organisation (ANSTO), Sydney, Australien; University of California, Davis, USA; Stanford University, Kalifornien, USA; Oak Ridge National Laboratory, Tennessee, USA; Inter-University Accelerator Centre, Neu-Delhi, Indien.

Das HZDR-IRO kooperierte mit dem Institut de Chimie Séparative de Marcoule (ICSM), Marcoule, Frankreich.

Das IFK kooperierte mit dem FRM II, Garching, Deutschland, DESY, Hamburg, Deutschland, der Christian-Albrechts-Universität zu Kiel, Deutschland und der University of California, Davis, USA.

Die Frankfurter Arbeitsgruppe kooperierte im Rahmen des Verbundvorhabens neben den Verbundpartnern mit mehreren Arbeitsgruppen am Los Alamos National Laboratory in New Mexico, USA (Material Science Gruppe von C. Stanek, Isotope Production Facility, Los Alamos Neutron Scattering Center), mit den Materialwissenschaftlern an der GSI (AG Trautmann), mit Gruppen an PETRA III/DESY, mit einer Theoriegruppe (Prof. K. Refson, Royal Holloway University, UK) und mit einem Softwareunternehmen (Accelrys/BioVia).

Das LUH-IRS kooperiert mit CHALMERS, Stockholm Schweden; Czech Technical University, Prag, Tschechien; National Nuclear Laboratory, UK; State Ecological Academy of Post-Graduate Education and Management (SEAPGEM), Kyiv; Paul-Scherer-Institut, Villigen, Schweiz sowie dem INE am KIT.

Diese Kontakte ermöglichten den Nachwuchswissenschaftlern im Rahmen von mehrtägigen oder sogar mehrwöchigen Gastaufenthalten die Gelegenheit, die bestehenden Kooperationen zu vertiefen, aber auch neue zu knüpfen.

Institut de Chimie Séparative de Marcoule (ICSM), Marcoule, Frankreich; Supervisor: Prof. Dr. Nicolas Dacheux

Joint Research Centre - Institute for Transuranium Elements (ITU), Karlsruhe; Supervisor: Dr. Karin Popa

Referenzen:

- [Belin2009] R.C. Belin, P.M. Martin, P.J. Valenza, A.C. Scheinost, *Inorg. Chem.*, 2009, 48, 5376.
- [Boatner1988] L.A. Boatner, B.C. Sales, In: W. Lutze, R.C. Ewing, (eds) "Radioactive waste forms for the Future", Amsterdam, North-Holland, 1988.
- [Chartier2001] A. Chartier, C. Meis, J.D. Gale, *Phys. Rev. B*, 2001, 64, 085110.
- [Donald1997] I.W. Donald, B.L. Metcalfe, R.N.J. Taylor, *J. Mater. Sci.*, 1997, 32, 5851.
- [Ewing1995] R.C. Ewing, W.J. Weber, W. Lutze, Final Proceedings „Plutonium stabilization & immobilization workshop“, 1995, 389.
- [Ewing2004] R.C. Ewing, W.J. Weber, J. Lian, *J. Appl. Phys.*, 2004, 95, 5949.
- [Ewing2006] G.R. Lumpkin, *Elements*, 2006, 2, 365.
- [Ewing2011] E.C. Ewing, *C.R. Geoscience*, 2011, 219.
- [Lutze1988] W. Lutze, R.C. Ewing, „Radioactive waste forms for the future“, (North-Holland, Amsterdam, 1988).
- [Martin2009] P.M. Martin, R.C. Belin, P.J. Valenza, A.C. Scheinost, *J. Nucl. Mater.*, 2009, 385, 126.
- [Oelkers2008] E.H. Oelkers, J.-M. Montel, *Elements*, 2008, 4, 113.
- [Oelkers2002] E.H. Oelkers, F. Poitrasson, *Chem. Geol.* 2002, 191, 73.
- [Weber1998] W.J. Weber, R.C. Ewing, C.R.A. Catlow, T. Diaz de la Rubia, L.W. Hobbs, C. Kinoshita, H.-J. Matzke, A.T. Motta, M. Nastasi, E.K.H. Salje, E.R. Vance, S.J. Zinkle, *J. Mater. Res.*, 1998, 13, 1434.
- [Weber2009] W.J. Weber, A. Navrotsky, S. Stefanovsky, E.R. Vance, E. Vernaz, *MRS Bulletin*, 2009, 34, 46.

2 Darstellung der Ergebnisse

2.1 Erzieltes Ergebnis

2.1.1 Structure of lanthanide phosphates

The large, distorted, 8 or 9-coordinated, $\text{LnO}_{8,9}$ polyhedra can connect to the small, relatively rigid PO_4 tetrahedra in three different ways and with a large variation in Ln-P distances, which is the major cause for the ability of these minerals to host a variety of (trivalent) cations and for their high resilience towards radiation damage similar to zirconia-based ceramics (Belin et al., 2009; Martin et al., 2009). Fig. 1 gives an overview of the three different lanthanide phosphate structure types monazite, rhabdophane and xenotime at the short-range order level observable by EXFAS spectroscopy.

Monoclinic anhydrous **monazite** (LnPO_4) forms with the early (and larger) lanthanides (La to Gd). The trivalent lanthanide cations in monazite are coordinated to nine O. The resulting strongly distorted LnO_9 polyhedra connect to two edge-sharing (ES) PO_4 tetrahedra, one double-corner-sharing (DCS) PO_4 tetrahedron, and four single corner-sharing (CS) PO_4 tetrahedra, spanning Ln-P distances from 3.22 to 3.82 Å. The LnO_9 polyhedra are not only connected through these PO_4 tetrahedra, but also share edges with 6 other LnO_9 units resulting in Ln-Ln distances of 4.10 to 4.40 Å.

Hydrous **rhabdophane** ($\text{LnPO}_4 \cdot n\text{H}_2\text{O}$) forms as an aqueous alteration product of monazite and hence hosts a similar range of early lanthanides (La to Dy) (Rafiuddin and Grosvenor, 2016). While a hexagonal structure was assumed from the first structure refinements on (Mooney, 1948, 1950), this was recently reassigned to a monoclinic space group (Mesbah et al., 2014). In contrast to the hexagonal structure with solely 8-fold coordination (1/3 of Ln positions), Ln cations are coordinated here also to nine O as in monazite (2/3 of Ln positions), while other important aspects of the short-range structure are very similar, including the linkage to two edge-sharing and four corner-sharing phosphate groups.

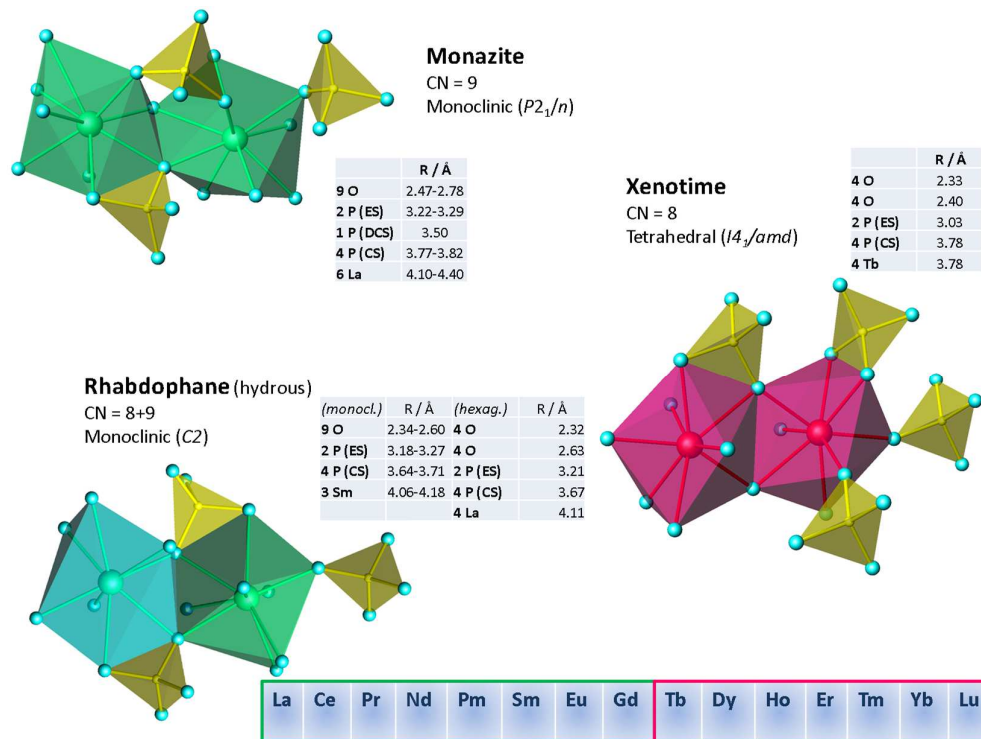


Fig. 1. Short-range structure of the three different types of lanthanide phosphates.

Finally, the tetrahedral **xenotime** (LnPO_4) structure forms with the smaller lanthanides Tb to Lu. Here, the La centers are coordinated to four shorter and four longer O atoms. Much shorter Ln-Ln distances

(3.78 Å for Tb) result from the edge-sharing of these eight coordinated LnO₈ polyhedra. The less strongly distorted LnO₈ polyhedra are also linked through phosphate units adopting two edge-sharing and four corner-sharing linkages similar to the rhabdophane structure.

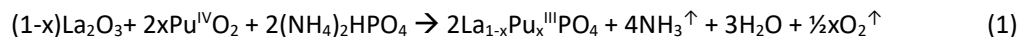
2.1.2 The local structure of Pu in La/Pu monazite solid solutions

Phosphate ceramics with monazite structure have been and are still the object of extensive research activities. These studies comprise investigations on the structure and properties and have been performed on the pure LnPO₄ endmembers and on solid solutions containing mainly surrogates for tri- and tetravalent actinides (An). In contrast, only a few studies on transuranic-bearing monazite materials are available in the literature. Am-, Cm- as well as Cf-, Bk-, and Es-phosphates have been synthesized and characterized (Bregiroux et al., 2007; Hobart et al., 1983; Keller and Walter, 1965; Rai et al., 1992). Monoclinic PuPO₄ was obtained originally by (Bjorklund, 1957) by precipitation of Pu^{IV}-oxalato phosphate followed by its thermal decomposition, as well as by dehydration of rhabdophane-like PuPO₄·nH₂O. The preparation of Pu^{III}PO₄-monazite via solid state synthesis from Pu^{IV}O₂ and NH₄H₂PO₄ in inert atmosphere was reported by (Bamberger et al., 1984) and (Bregiroux et al., 2007). Recently the refined crystal structure and oxidation state +III of PuPO₄ samples derived by solid state reaction have been solved by Rietveld analysis of XRD data and high resolution X-ray Absorption Near Edge Structure (XANES) spectroscopy, respectively (Popa et al., 2016). The thermal behavior of Pu^{III}PO₄, such as lattice parameter evolution and decomposition was studied by (Jardin et al., 2008).

The solid state synthesis route has already been adopted successfully to synthesize La_{1-x}Pu_xPO₄ (x = 0.01 – 0.1) solid solutions by (Popa et al., 2007) and (Zhang and Vance, 2008). XRD analysis for all compositions revealed single-phase materials with monoclinic structure and the oxidation state +III of Pu was confirmed by diffuse reflectance spectroscopy. Finally for self-irradiation studies PuPO₄ (7.2 wt% ²³⁸Pu) and (La,Pu)PO₄ (8.1 wt% ²³⁸Pu) were synthesized by wet chemical method based on precipitation from aqueous nitrate solutions by (Burakov et al., 2004). However, the incorporation of pure Pu^{IV} by coupled substitution into a monazite-cherelite system Ln_{1-x}Ca_{0.5x}Th_{0.5x}PO₄ as well as the synthesis of pure CaPu^{IV}PO₄ failed so far. Instead (Bregiroux et al., 2007) and (Deschanel et al., 2006) prepared mixed-valence compounds such as Pu_{0.4}^{III}Pu_{0.3}^{IV}Ca_{0.3}PO₄ and Ca_{0.09}Pu_{0.09}La_{0.73}Th_{0.09}PO₄, respectively.

Solid-state chemistry methods play an important role regarding the immobilization of existing separated inventories of Pu as it is stored intermediately as PuO₂. Wet chemistry methods such as precipitation may offer some advantages over the solid-state route with respect to the safe handling of radionuclides and minimization of contamination risk due to dust formation. However, the merits vanish taking into account the efforts needed to dissolve the hardly soluble PuO₂ in glove boxes. Hence, within this work the structural incorporation and loading limitations of Pu^{III} in monazite-type phosphate ceramics by solid-state synthesis using PuO₂ as starting material has been investigated systematically for the first time. The refined crystal structure of the (La,Pu)PO₄-monazite solid solutions has been studied by a combination of XRD and EXAFS. Particular attention has been paid to the determination of the valence state of plutonium in the solid solution using XANES since Pu⁴⁺O₂ has been used as precursor material for the solid solution preparation under inert atmosphere.

Powder X-ray diffraction. The conventional solid-state method, reported previously for synthesis of Pu^{III}PO₄ with monazite structure, was applied in this work to obtain La_{1-x}Pu_xPO₄ monazite solid solutions according to the equation (1).



PXRD patterns of the resulted compounds with the corresponding references from COD (Crystallography Open Database) are shown in Fig. 2.

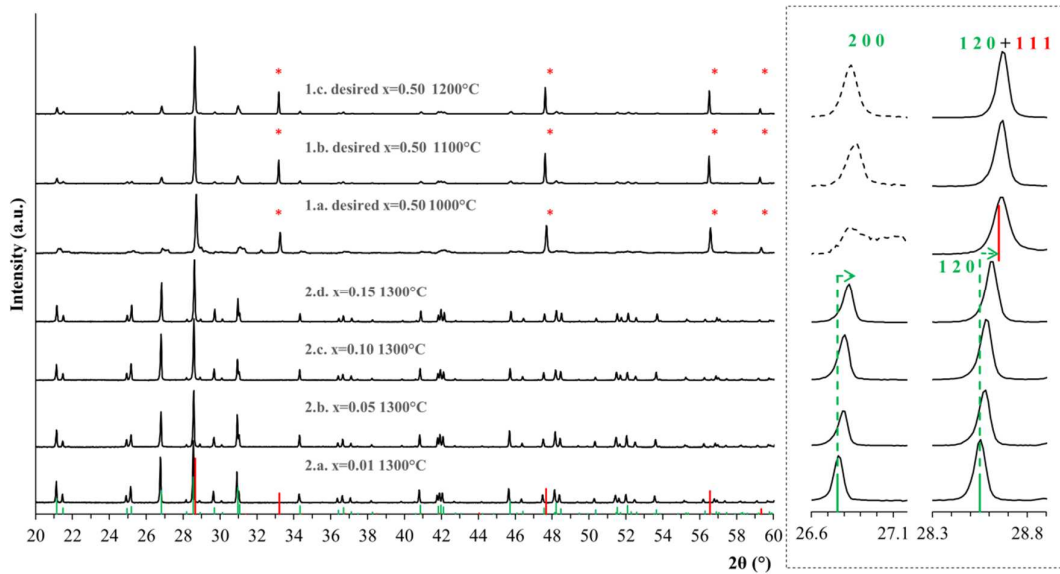
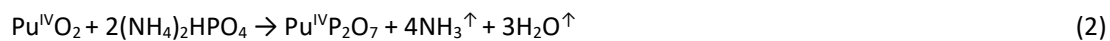


Fig. 2. Diffraction patterns of the synthesized $\text{La}_{1-x}\text{Pu}_x\text{PO}_4$ compounds with $x = 0.01, 0.05, 0.1, 0.15, (0.50)$ with the corresponding references from COD (Crystallography Open Database) for the LaPO_4 -monazite (green) and PuO_2 (red). Red stars highlight the characteristic Bragg reflections of the PuO_2 phase. The [200] and [120] reflections of the monazite phase are shown in the insert. The [200] Bragg reflections marked with the dashed line are magnified by factor 7 relatively to the corresponding diffraction patterns.

According to the XRD data, the first attempt to synthesize $\text{La}_{0.50}\text{Pu}_{0.50}\text{PO}_4$ solid solution by the conventional solid state method at 1000°C , led to the formation of several phases: $(\text{La},\text{Pu})\text{PO}_4$ monazite solid solutions with varying Pu-loadings and a cubic PuO_2 phase. The corresponding diffraction pattern is shown in Fig. 2, red stars highlight the characteristic Bragg reflections of the PuO_2 phase. The splitting of the [200] Bragg reflections of the monazite phase indicates the formation of at least two monazite phases with different molar fractions of Pu. A similar effect was already observed by (Bregiroux et al., 2006) for mixed lanthanide orthophosphates. It seems to be challenging to obtain a pure and homogeneous monazite phase of mixed orthophosphates by a solid-state method due to the unequal reaction temperature for different cations. By increasing the synthesis temperature up to 1100 and 1200°C a single solid solution with monazite structure was obtained, but the PuO_2 Bragg reflections remained evident, too (Fig. 2). The phase ratio and lattice parameters of the monazite phase were determined using Rietveld refinement of the XRD data. The increase of temperature from 1100 to 1200°C led to increase of the monazite phase fraction by 5% reaching $86\pm 1\%$. However, the molar fraction of Pu remained constant within the uncertainties of the refinement (0.15 ± 0.03 and 0.22 ± 0.05 , respectively). No further heating has been applied, bearing in mind the thermal behavior of PuPO_4 end member.

Apparently the unequal reaction temperatures for lanthanum and plutonium oxides are caused by the reduction of Pu^{4+} during the solid state synthesis. The mechanism of the redox reaction comprises a two-step mechanism. First, in an intermediate step a tetravalent plutonium pyrophosphate is formed that subsequently decomposes according to the equations (2) and (3):



The Pu^{IV} to Pu^{III} redox-reaction may inhibit the formation of a pure single-phase monazite-type $\text{La}_{1-x}\text{Pu}_x\text{PO}_4$ solid solution by the solid-state reaction, especially at higher Pu-content. Moreover, it explains the presence of residual PuO_2 after solid-state reaction. A thermal decomposition of PuPO_4 at 1200°C in inert atmosphere according to (Jardin et al., 2008):



can definitely be excluded because in detailed evaluation of the XRD patterns no Pu_2O_3 was found. Therefore, the residual PuO_2 appears to be unreacted and not reduced precursor material of the synthesis. The formation of a single-phase solid solution bearing a higher Pu content can be expected by optimizing the synthesis parameters in terms of the excess of $(\text{NH}_4)_2\text{HPO}_4$. Additionally, $\text{La}_{1-x}\text{Pu}_x\text{PO}_4$ solid solutions with relatively low molar fraction of Pu might be stabilized by the high thermal stability of the LaPO_4 matrix (melting temperature 2000°C) that would allow for solid-state reactions at a temperature above the decomposition temperature of pure PuPO_4 .

Based on these considerations the planned molar fraction of Pu was reduced and pure-phase $\text{La}_{1-x}\text{Pu}_x\text{PO}_4$ solid solutions with monazite structure were successfully obtained at 1300°C for the compositions with $x = 0.01, 0.05, 0.10, 0.15$ according to the PXRD data (Fig. 2). No characteristic Bragg reflections for PuO_2 are evident in the PXRD patterns. The insert of Fig. 2 demonstrates exemplarily the linear shift of the [200] and [120] Bragg reflections towards higher 2θ values on increasing the Pu-loading. This effect is caused by the lattice contraction due to the incorporation of the slightly smaller Pu^{3+} ions compared to La^{3+} (1.187 \AA and 1.215 \AA , respectively, for nine-fold coordination). As a consequence the lattice parameters decrease linearly as a function of Pu-content confirming solid solution formation according to the Vegard's law (Fig. 3). The reaction to form solid solution appears to be more favorable from a kinetic point of view compared to the plutonium phosphate decomposition which is possible at 1300°C . PuPO_4 seems to be stabilized at this temperature due to the incorporation into the lattice of the LaPO_4 host matrix forming a solid solution.

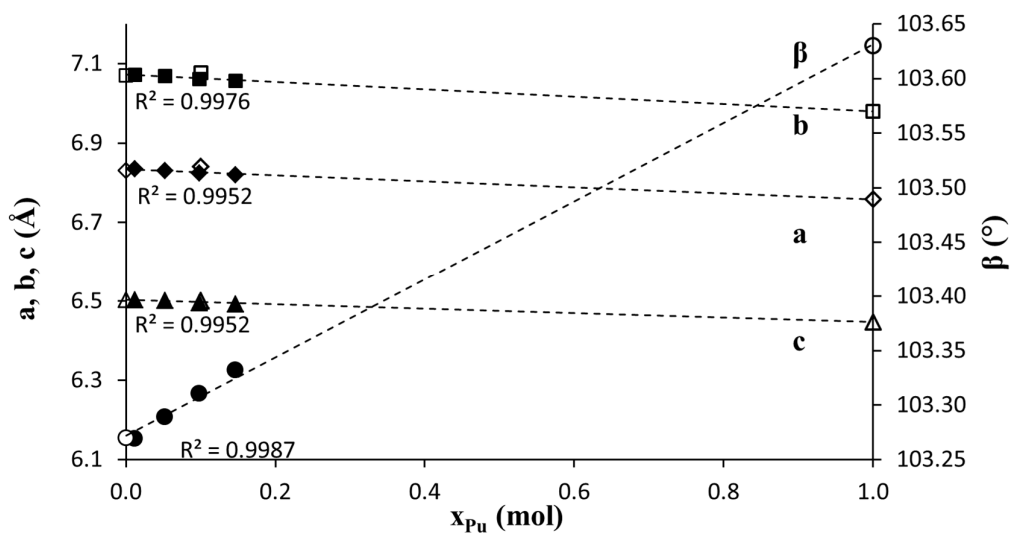


Fig. 3. Evolution of the lattice parameters of the $\text{La}_{1-x}\text{Pu}_x\text{PO}_4$ solid solutions with monazite structure ($x = 0-1$). Lattice parameters for LaPO_4 ,⁵ PuPO_4 ³ as well as for $\text{La}_{0.9}\text{Pu}_{0.1}\text{PO}_4$ ⁴⁴ are marked with open symbols.

Scanning electron microscopy with energy dispersive spectroscopy. The chemical composition and the microstructure of the single phase solid solutions have been investigated using SEM-EDS. The EDS analysis confirmed the homogeneity of the samples as well as the actual compositions of the synthesized solid solutions (ratio La-Pu-P). The data are summarized in Table 1.

Table 1: Pu content derived from EDS measurements.

Sample	Mol%			x(Pu)
	La	Pu	P	
La _{0.99} Pu _{0.01} PO ₄	0.51	0.01	0.38	0.01 ^a
La _{0.95} Pu _{0.05} PO ₄	0.54	0.03	0.38	0.04 ^b
La _{0.90} Pu _{0.10} PO ₄	0.52	0.06	0.44	0.1 ^a
La _{0.85} Pu _{0.15} PO ₄	0.48	0.08	0.42	0.14 ^b

Mean value from ^a3 and ^b2 measurements.

The SEM-micrographs in Fig. 4 show the microstructures of the selected compounds with $x = 0.01$ and $x = 0.15$ at different magnifications. The sponge-like microstructure of the samples indicates a vigorous reaction during the heat treatment accompanied by active gas release. These observations verify self-homogenization of the reaction mixture during the heat treatment. The average grain diameter for each composition determined from the corresponding SEM micrographs is presented in Fig. 4 as a function of composition. It is noticeable, that the grain sizes for the composition with the molar fraction of plutonium $x = 0.15$ are larger whereas its porosity is smaller in comparison to those for $x = 0.01$. A linear increase in the average grain diameter with increasing molar fraction of plutonium was observed. It suggests that Pu content lowers the operable sintering temperature of the solid solutions.

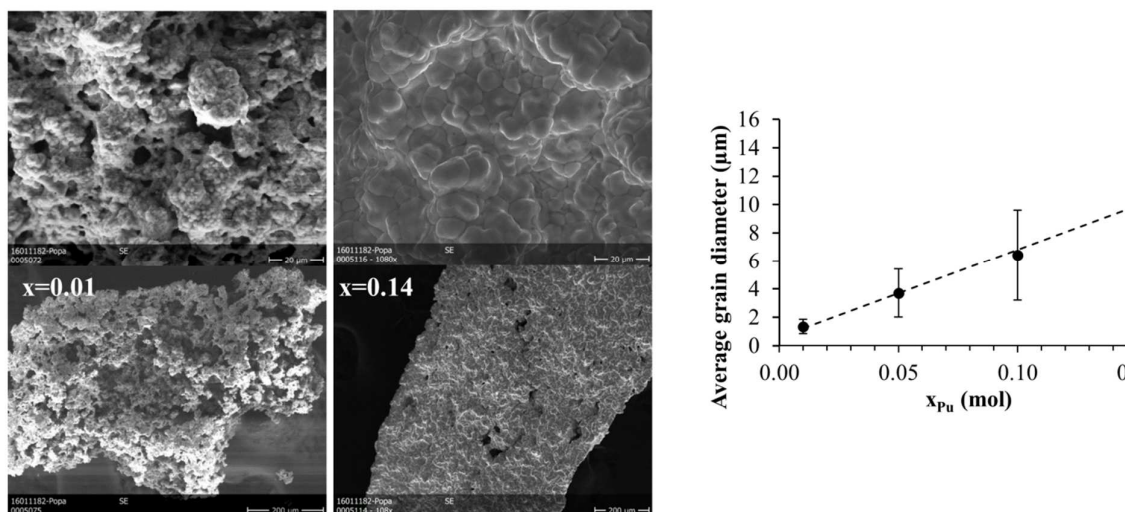


Fig. 4. SEM images of microstructure (a) and average grain diameters (b) of the La_{1-x}Pu_xPO₄ solid solutions with monazite structure in dependence on composition. The apparent increasing error bars with increasing Pu content represent the uncertainties of a grain size distribution.

X-ray absorption spectroscopy. Here we studied the oxidation state and the local environment of the incorporated Pu atoms in the crystal structure as a function of composition of the synthesized solid solutions ($x = 0.01, 0.04, 0.10, 0.14$) by XANES (X-ray absorption near-edge structure) and EXAFS (extended X-ray absorption fine-structure) spectroscopy, respectively.

The Pu-L₃ edge X-ray absorption near-edge structure (XANES) spectra of the synthesized solid solutions ($x = 0.01, 0.04, 0.10, 0.14$) are presented in Fig. 5. The white line position of the solid solutions matches that of the purely trivalent monazite endmember ($x=1.00$), and is about 5 eV lower than that of the Pu^{IV} reference, PuO₂. A subsequent analysis of the spectral series by iterative transformation factor analysis (ITFA) (Rossberg et al., 2003) confirmed that all samples contain at least 95% of Pu^{III}, as expected for the synthesis under inert atmosphere (Jardin et al., 2008).

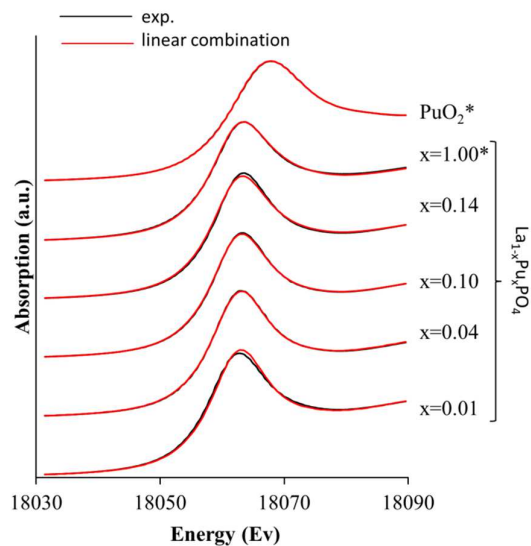


Fig. 5. Experimental Pu-L₃ XANES spectra (black) and their reproduction (red) by the two reference spectra show on top (Pu^{III} and Pu^{IV}).

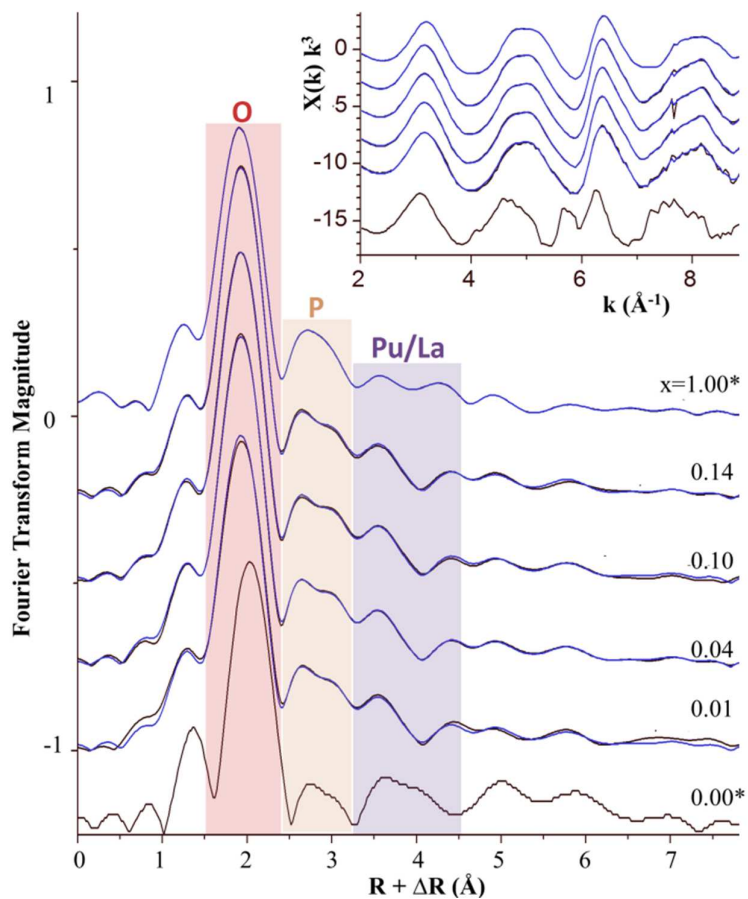


Fig. 6. Pu-L₃ EXAFS spectra of Pu monazite and Pu-La monazite solid solutions in comparison to the La-L₃ EXAFS spectrum of La monazite. Experimental data are given as black lines, blue lines are the reconstruction of the Pu-L₃ spectra by two principal components. The large figure gives the k^3 -weighted Fourier transform magnitudes (FTM), the insert the k^3 -weighted chi-spectra. Major contributions from the nine coordinating oxygen atoms are within the red area, those of the seven nearest phosphorous atoms are within the orange area, and those of the six nearest Pu/La atoms are within the purple area..

Fig. 6 shows from top to bottom the Pu L_{III} -edge Fourier transform magnitudes (FTM) of the pure Pu-monazite endmember, of the Pu-doped La-monazite samples sorted along decreasing Pu atom-percentage, and finally the La- L_{III} spectrum of the pure La-monazite endmember. The FTM of the Pu-La series are almost identical independent of Pu-doping; while the FTM of pure Pu-monazite has distinct features in the regions of the next P neighbours (marked in orange) and of the next Pu/La neighbours (marked in purple). In contrast, the spectrum of $LaPO_4$ shows a longer distance of the oxygen coordination shell (red), in addition to different peak shapes in the P and Pu/La regions.

With space group $P 1 21/n 1(14)$, the monazite structure shows poor radial distribution ordering of the atoms around the cation centers. In $LaPO_4$, for instance, the coordination shell of nine oxygen atoms has La-O distances (R_{La-O}) ranging from 2.45 to 2.78 Å; the seven P atoms from the phosphate units directly linked to this LaO_9 polyhedron have distances ranging from 3.20 to 3.79 Å, followed by 3 La neighbors from 4.08 to 4.15 Å and another three La neighbors from 4.30 to 4.36 Å. Since the distal resolution of EXAFS is limited by $\pi/(2\Delta\chi)$, shells have to be separated by at least 0.21 Å, given the limited k-range available (2.0 to 9.5 Å⁻¹). Therefore, the different individual interatomic distances had to be grouped into shells for EXAFS fitting. The most stable fits were obtained with the following grouping: a coordination shell of 9 oxygen atoms, 3 shorter and 4 longer cation-P distances, 3 shorter and 3 longer cation-cation distances. The results derived from the corresponding fits are shown in Table 2.

In all Pu-containing monazites, the coordination shell could be fitted with 9 Pu-O paths, giving average distances of 2.47 to 2.48 Å and a relatively high disorder expressed by Debye-Waller factors of ~ 0.01 Å² in line with the expected distorted tricapped prism structure (Table 2). For $LaPO_4$, this distance is significantly larger (2.53 Å), owing to the larger ionic radius of La^{3+} versus Pu^{3+} . Furthermore, the two Pu-P paths provided distances at 3.20 and 3.74 Å, with no significant change of distances or disorder from 100% to 1% Pu.

For $PuPO_4$, the following two Pu-Pu shells were fitted with average distances of 4.07 and 4.24 Å, well in line with the monazite structural model. For the Pu-La solid solution series, however, the backscattering elements of the shorter and longer cation-cation interactions may be La or Pu, with a prevalence of Pu-Pu for high Pu content, and a prevalence of Pu-La for lower Pu. We tried to identify the prevalent backscattering element by wavelet analysis (Funke et al., 2005), but could not distinguish contributions from La and Pu due to the k range (2.0 to 9.5 Å⁻¹) limited by the presence of about 2% of the Am daughter nuclide. We therefore tried different combinations of Pu-Pu and Pu-La paths. For all samples, with Pu ranging from 1 to 15 atom-%, the best fit was obtained with Pu-Pu paths for the shorter, and Pu-La paths for the longer distance. This may be an indication for an inhomogeneous distribution of Pu in the La-Pu-monazite lattice, i.e. a certain clustering of Pu cations, which changes little as is revealed by the invariant FTM pattern in the La/Pu region. With R_{Pu-Pu} between 4.05 and 4.10 Å, the solid solution samples do not vary significantly from the distance of 4.07 Å found for the pure $PuPO_4$ endmember, further supporting the clustering of Pu atoms. In contrast, the Pu-La distances at 4.33 Å are significantly longer than the corresponding Pu-Pu distance of 4.24 Å in $PuPO_4$, and similar to the La-La distance in $LaPO_4$.

In conclusion, the local environment of Pu remains $PuPO_4$ -like along the solid solution series, except for the longest fitted cation-cation distance, which is always $LaPO_4$ -like. Such an effect is most consistently explained by clustering, i.e. a heterogeneous distribution of cations in solid solutions at the molecular scale, which is observable by short-range probes like EXAFS, but not by long-range probes like XRD as was observed for instance for metal oxides, silicates and phosphates (Ellis et al., 2006; Hazemann et al., 1992; Henderson et al., 2001; Martin et al., 2007; Scavini et al., 2012; Scheinost et al., 1999; Scheinost et al., 2001; Vantelon et al., 2003) Even more relevant, a similar effect was recently observed by EXAFS for (La,Eu) PO_4 and Cm-doped (La,Gd) PO_4 monazite solid solutions, where Eu or Gd served as inactive surrogates for trivalent actinides. For both solid solution series bond lengths in the local environment of Eu and Cm respectively were significantly shorter in comparison to those in the local environment of La. This indicates that the local environment of La with relatively longer and therefore weaker bonds is adjusting by the incorporation of smaller cations in the $LaPO_4$ monazite matrix.

Table 2. EXAFS shell fit results of Pu-doped La-monazites in comparison to PuPO₄ and LaPO₄ (Pu-L_{III} and La-L_{III} spectra, respectively).

Sample	Path	CN	R [Å]	σ ² [Å ²]	ΔE ₀ [eV]	S ₀ ²	χ _{res} [%]
PuPO ₄ (T)	Pu-O	9	2.47	0.0103	9.9	0.70	7.4
	Pu-P	3	3.21	0.0117			
	Pu-P	4	3.74	0.0105			
	Pu-Pu	3	4.07	0.0061			
	Pu-Pu	3	4.24	0.0057			
La _{0.85} Pu _{0.15} PO ₄ (T)	Pu-O	9	2.48	0.0094	9.2	0.77	6.3
	Pu-P	3	3.20	0.0122			
	Pu-P	4	3.75	0.0083			
	Pu-Pu	3	4.10	0.0014			
	Pu-La	3	4.33	0.0010			
La _{0.90} Pu _{0.10} PO ₄ (T)	Pu-O	9	2.48	0.0098	8.9	0.79	6.3
	Pu-P	3	3.20	0.0125			
	Pu-P	4	3.74	0.0085			
	Pu-Pu	3	4.05	0.0016			
	Pu-La	3	4.32	0.0010			
La _{0.95} Pu _{0.05} PO ₄ (T)	Pu-O	9	2.48	0.0094	8.8	0.78	6.6
	Pu-P	3	3.20	0.0130			
	Pu-P	4	3.74	0.0082			
	Pu-Pu	3	4.06	0.0014			
	Pu-La	3	4.33	0.0010			
La _{0.99} Pu _{0.01} PO ₄ (F)	Pu-O	9	2.48	0.0100	9.2	0.74	7.6
	Pu-P	3	3.20	0.0112			
	Pu-P	4	3.74	0.0083			
	Pu-Pu	3	4.06	0.0012			
	Pu-La	3	4.33	0.0010			
LaPO ₄ (F)	La-O	9	2.53	0.0106	10.2	0.63	13.8
	La-P	3	3.31	0.0205 ^c			
	La-P	4	3.73	0.0205 ^c			
	La-La	3	4.08	0.0082 ^c			
	La-La	3	4.38	0.0082 ^c			
LaPO ₄ (XRD)	La-O	9	2.56				
	La-P	3	3.32				
	La-P	4	3.76				
	La-La	3	4.11				
	La-La	3	4.32				

CN: coordination number, R: radial distance, σ²: Debye-Waller term, ΔE₀: phase shift, S₀²: amplitude reduction factor, χ_{res}: residual error, c: parameters were correlated during the EXAFS fit, T, F: EXAFS data collected in transmission or fluorescence mode, respectively

Resume. Single-phase La_{1-x}Pu^{III}_xPO₄-monazite solid solutions with molar fraction of Pu up to x = 0.15 were synthesized by a solid state method at 1300°C. At a higher Pu content (x = 0.5) residues of unreacted PuO₂ were detected: Due to the absence of Pu₂O₃, however, decomposition of PuPO₄ or the associated solid solution can be excluded. Moreover the formation of single phase solid solutions with high Pu content can be obtained after optimization of the synthesis method. XRD and SEM analysis revealed that the solid solutions are single phased and homogeneous. X-ray absorption spectroscopy

analysis of the single phase (La,Pu)PO₄ solid solutions at the Pu-L₃ and La-L₃ edges proves the incorporation of Pu^{III} into defined lattice sites of the monazite structure and indicates clustering of few Pu atoms in the La-Pu-monazite lattice. Comparison of XRD and EXAFS data reveals adjusting of LaPO₄ local environment by incorporation of Pu, whereas the local environment of Pu remains PuPO₄-like for the entire solid solution range. This work demonstrates that monazite-type ceramics can be fabricated with a significant amount of Pu (10-15%) by conventional solid state reaction at 1300°C, thereby demonstrating the high potential of such materials for nuclear waste applications (Arinicheva et al., submitted).

This work has been performed in close cooperation with FZJ-IEK6 (02NUK021A) and has been used to prepare the following article:

Arinicheva, Y., Popa, K., Scheinost, A.C., Rossberg, A., Dieste-Blanco, O., Raison, P., Cambriani, A., Neumeier, S., Somers, J., Dirk and Bosbach (submitted) Structural investigations of (La,Pu)PO₄ monazite solid solutions: XRD and XAFS study. Journal of Nuclear Materials.

2.1.3 The local structure of La and Eu in La/Eu monazite solid solutions

Experimental. EXAFS measurements were carried out at the Rossendorf Beamline (ROBL), located at BM20 of the European Synchrotron Radiation Facility (ESRF; Grenoble, France) which operated at 6 GeV and 130-200 mA. At ROBL, a pair of Si (111) crystals for monochromatization and a pair of Si mirrors were applied for vertical beam collimation and suppression of higher harmonics. EXAFS spectra were collected at La L₁ (6266 eV) and Eu L₃ (6977 eV) edges, using 30 cm of ionization chambers filled at ambient pressure with a gas mixture of 60% He and 40% N₂ for I₀ and 100% N₂ for I₁/I₂. Energy calibration was set as the maximum of the first derivative of vanadium foil at 5464 eV. All the samples were measured in transmission mode at 15 K, using a close-cycle He cryostat to improve signal quality by suppressing thermal contributions to the Debye Waller factor (DW). Data reduction and extraction of EXAFS oscillation was deduced using Athena code (Ravel and Newville, 2005). The threshold energy, E₀, was defined as the maximum of the first derivative of the absorption coefficient. Experimental EXAFS spectra were Fourier transformed using a Hanning window over the *k*-space ranges of 2.0 - 9.6 Å⁻¹ for La and 2.0 - 12.0 Å⁻¹ for Eu. Theoretical phase shifts and backscattering amplitudes were obtained from FEFF9.6 (Ankudinov and Rehr, 1997) using LaPO₄ and EuPO₄ structures reported in the literature (Ni et al., 1995). The theoretical calculation of both structures was carried out with a radius cluster of 6 Å, taking single scattering (SS) and multiple scattering (MS) paths. The fitting was performed in R-space using *k*¹, *k*², *k*³ weights for La and Eu. Similar to the model approach shown for the Pu/La monazite EXAFS shell fits (chapter 2.1.2), the following single scattering paths were used for fitting: La-O, La-Ln_s, La-Ln_i, La-P, Eu-O, Eu-Ln_s, Eu-Ln_i, La-P (Fig. 7). The distances (R), Debye-Waller (DW) factors, threshold energy (ΔE) were treated as free parameters; while the coordination numbers (CN) were constrained to the monazite model. The amplitude reduction factor, S₀², for the La L₁-edge was obtained from the fit of LaPO₄ and then kept constant for the fit of the solid solutions; for the fits of the Eu L₃-edge, S₀² was obtained from EuPO₄ and then also kept constant.

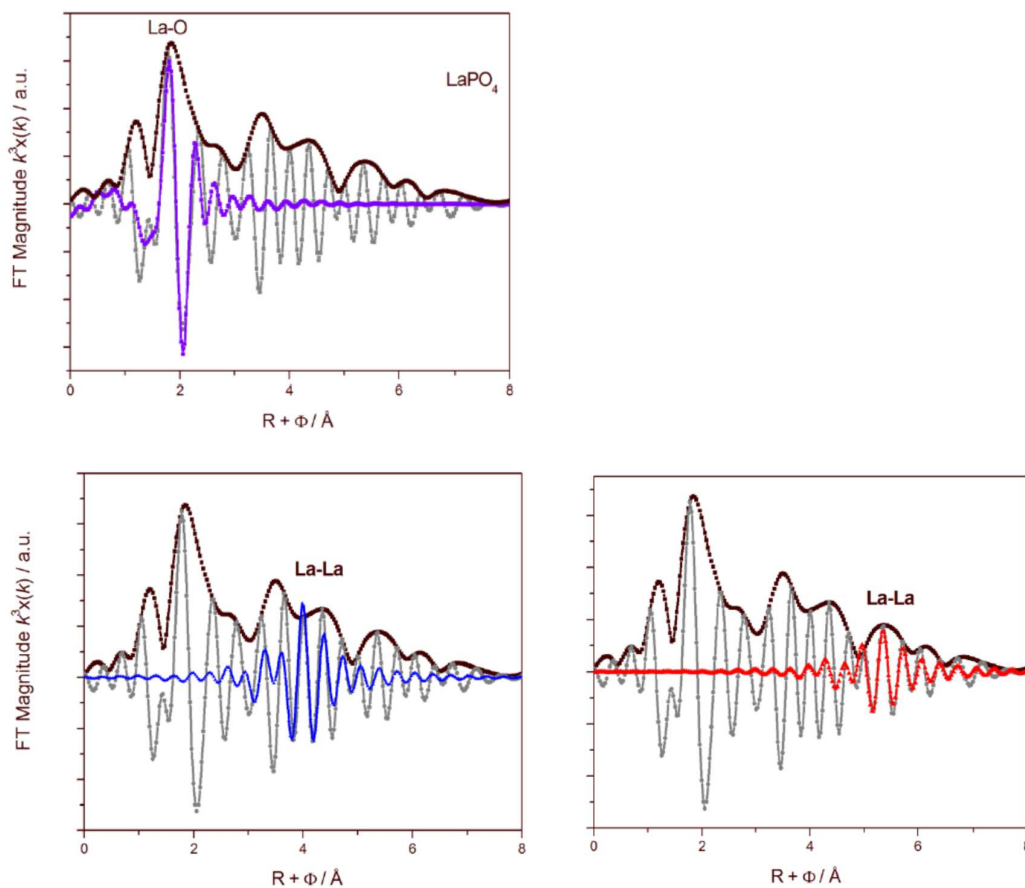


Fig. 7. Contributions of the La-O, short La-La and long La-La single scattering paths to the experimental EXAFS spectrum of LaPO₄.

Results. PXRD showed the sole presence of the monazite structure and an ideal solid-solution behavior of the La_{1-x}Eu_xPO₄ solid solution series, i.e. a linear shrinkage of the unit cell volume with increasing transition from La to Eu occupation (Fig. 8), which was also confirmed by ab initio calculations (Kowalski et al., 2017). The EXAFS spectra collected at the La L₁ and the Eu L₃-edges of the endmembers and the solid solutions show little changes, suggesting a monazite-type local structure for all samples (Fig. 9 and Fig. 10).

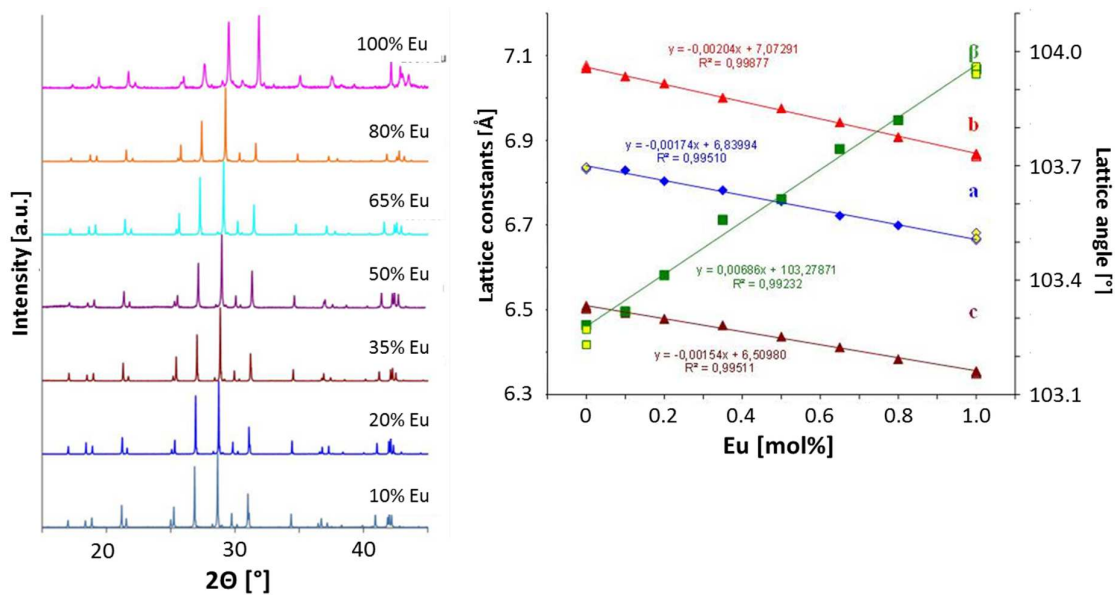


Fig. 8. PXRD patterns and unit cell dimensions of the $\text{La}_{1-x}\text{Eu}_x\text{PO}_4$ solid solution series

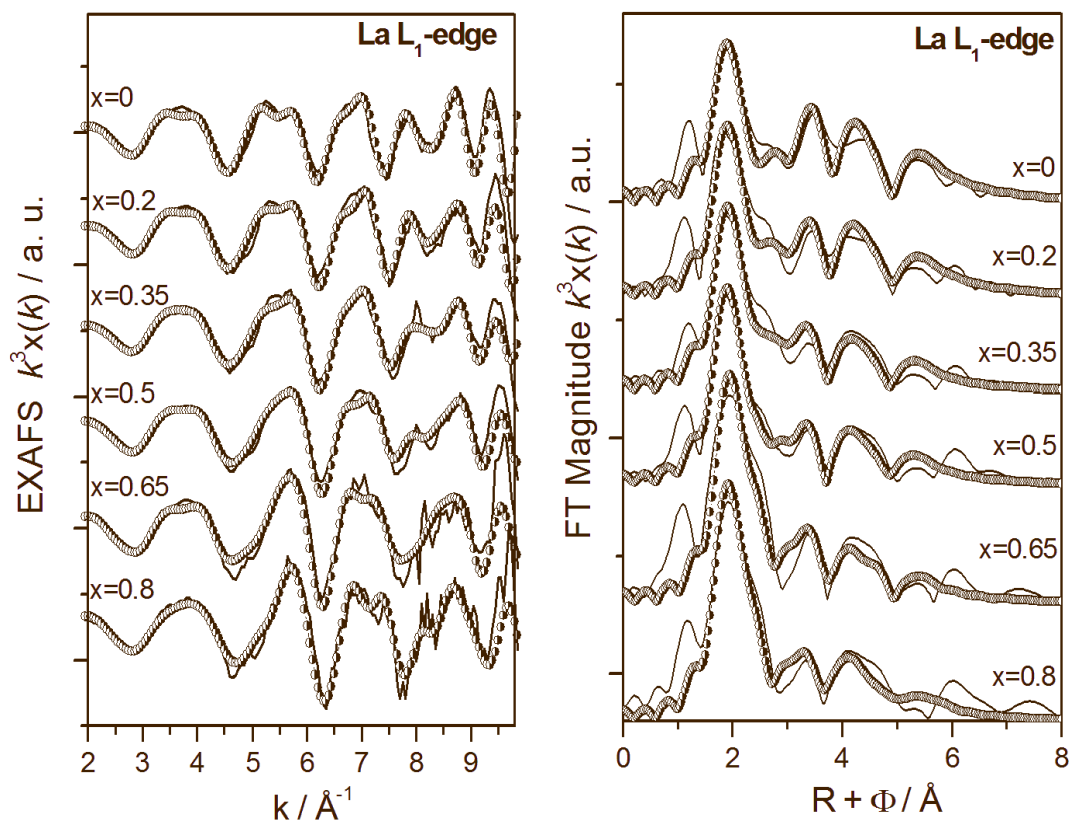


Fig. 9. $\text{La } L_1$ -edge EXAFS spectra of the La/Eu monazite solid solution (Experimental data in lines, and fits in dotted lines).

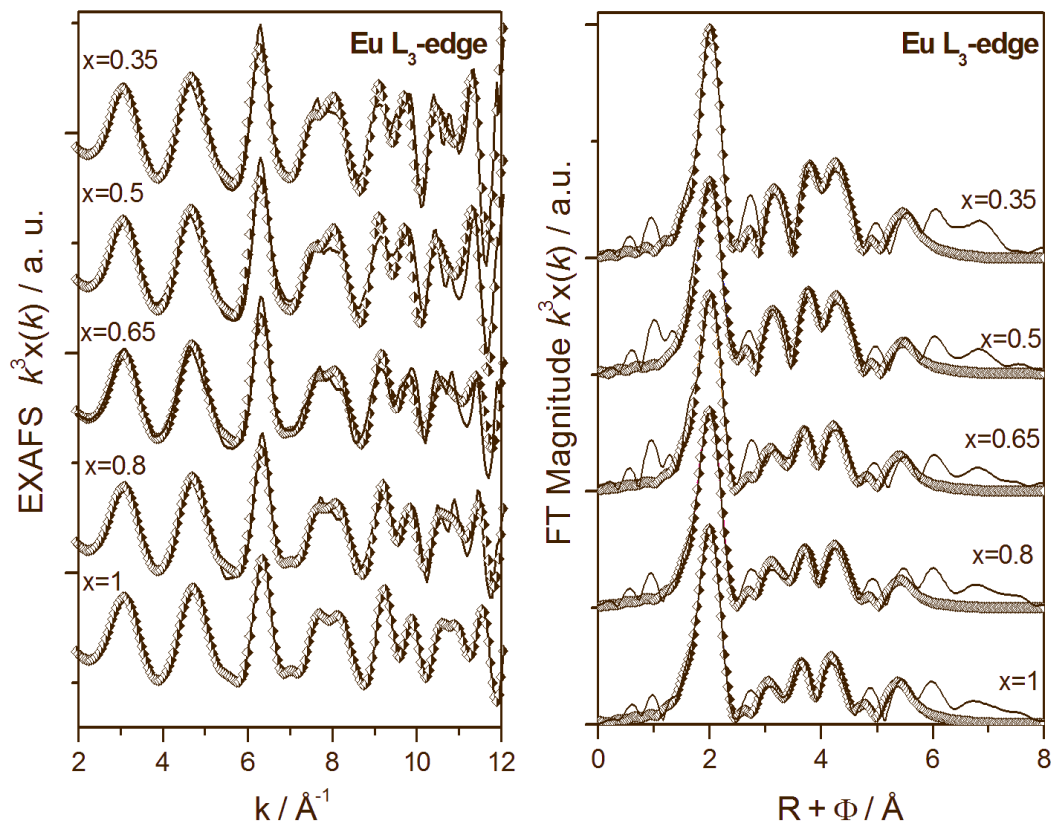


Fig. 10. Eu L_3 -edge EXAFS spectra of the La/Eu monazite solid solution (Experimental data in lines, and fits in dotted lines).

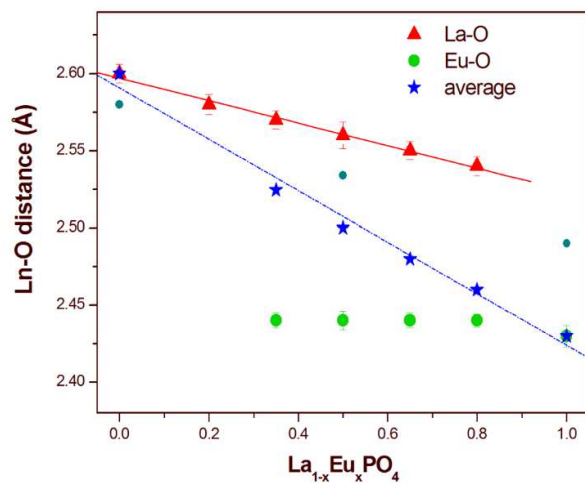


Fig. 11. EXAFS-derived La-O and Eu-O distances in La/Eu monazite solid solutions.

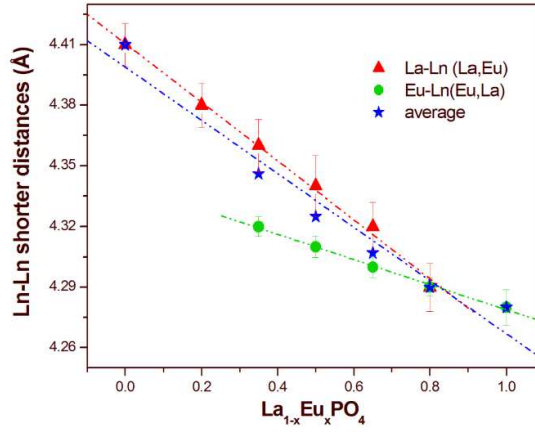


Fig. 12. EXAFS-derived short La-(La,Eu) and Eu-(La,Eu) distances in La/Eu monazite solid solutions.

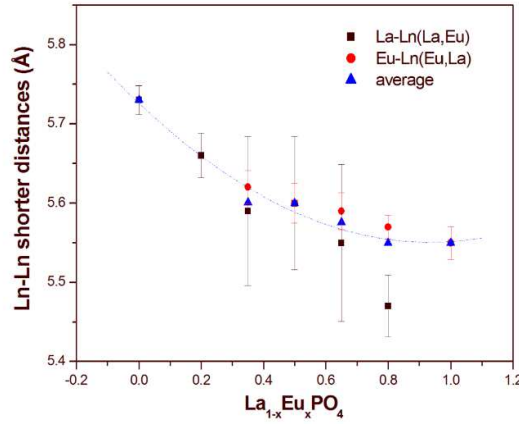


Fig. 13. EXAFS-derived long La-(La,Eu) and Eu-(La,Eu) distances in La/Eu monazite solid solutions.

Table 3. EXAFS fit results of the $La_{1-x}Eu_xPO_4$ solid solution series measured at La-L₁ and Eu-L₃ edges.

x	La-O		Eu-O		La-P / Å		Eu-P / Å	
	R/Å	$\sigma^2/\text{Å}^2$	R/Å	$\sigma^2/\text{Å}^2$	R/Å	$\sigma^2/\text{Å}^2$	R/Å	$\sigma^2/\text{Å}^2$
0.00	2.57	0.0072			3.37	0.0045		
0.20	2.56	0.0062			3.33	0.0055		
0.35	2.55	0.0053	2.41	0.0040	3.31	0.0063	2.74	0.0057
0.50	2.53	0.0047	2.41	0.0060	3.26	0.0078	2.71	0.0037
0.65	2.54	0.0031	2.41	0.0057	3.24	0.0027	2.71	0.0066
0.80	2.52	0.0028	2.41	0.0057	3.22	0.0030	2.70	0.0078
1.00			2.41	0.0060			2.69	0.0073
x	La-Ln _s		Eu-Ln _s		La-Ln _l		Eu-Ln _l	
	R/Å	$\sigma^2/\text{Å}^2$	R/Å	$\sigma^2/\text{Å}^2$	R/Å	$\sigma^2/\text{Å}^2$	R/Å	$\sigma^2/\text{Å}^2$
0.00	4.77	0.0008			5.74	0.0008		
0.20	4.75	0.0008			5.66	0.0008		
0.35	4.73	0.0043	4.31	0.0012	5.59	0.0043	5.63	0.0029
0.50	4.69	0.0040	4.29	0.0021	5.61	0.0040	5.61	0.0046
0.65	4.70	0.0050	4.27	0.0035	5.57	0.0050	5.60	0.0055
0.80	4.65	0.0039	4.26	0.0032	5.48	0.0039	5.58	0.0043
1.00			4.24	0.0030			5.55	0.0034

The fitted distances, however, reveal small, but consistent trends as a function of x (Fig. 11, Fig. 12, Fig. 13, Table 3). The La-O distances (red triangles) show a linear contraction with increasing Eu content, while the Eu-O distances remain invariant (green dots). A similar trend is shown by the shorter Ln-Ln distances, where most of the structural contraction with increasing Eu is due to the La-(La,Eu) nearest distances, while the Eu-(La,Eu) distances vary much less. It is therefore the local environment around La which buffers most of the long-range unit cell contraction, while the local environment around the much smaller Eu cation remains much more invariant. Only for the long Ln-Ln distance, both La and Eu environments behave similar, approaching the trend seen for the long-range order by PXRD.

This work has been performed in close collaboration with 02NUK021B. An article is in preparation.

2.1.4 The local structure of Cm in Cm³⁺-doped La_{1-x}Gd_xPO₄ monazite

Cm³⁺-doped (50 ppm) LaPO₄ and GdPO₄ end-members as well as La_{1-x}Gd_xPO₄ solid solutions with the compositions x = 0.0, 0.5, 1.0 were synthesized and characterized by XAFS spectroscopy on ROBL, supplementing their characterization by XRD (FZJ) and TRLFS (HZDR) (Fig. 14). The XANES spectra have an inflexion point at 18,972 eV and a white line maximum at 18,978 eV (calibrated against the Zr K-edge at 17,998 eV) in line with Cm^{III} (Bouty et al., 2016; Hennig et al., 2010). The EXAFS signal is dampened by self absorption effects, and the noise level is high due to the low Cm concentration. Nevertheless, the Fourier transform magnitudes of all three samples show a backscattering peak at about 2 Å (uncorrected for phase shift) assignable to the Cm-O coordination (marked in red). Fitting of this peak showed a contraction from 2.46 to 2.43 Å with increasing Gd-for-La substitution (Table 4). This contraction is in line with the decreasing size of the monazite unit cell when going from the larger La³⁺-bearing host toward the smaller Gd³⁺ bearing host.

The fitting results also show that the Debye-Waller (DW, σ^2) factor (which is an indicator for thermal and structural disorder) decreases from 0.0090 Å² in LaPO₄ to 0.0063 Å² in GdPO₄, while it is substantially larger for the solid-solution between both phases (0.0120 Å²). The differences in the DW factors between the monazite end-members can be ascribed to a larger mismatch between host and dopant radii causing a larger distortion of the monazite crystal lattice around the trivalent dopant. The cation radii of nine-fold coordinated La³⁺, Cm³⁺, and Gd³⁺ are 121.6 Å, 114.6 Å, and 110.7 Å, respectively. Thus, the larger mismatch of host and dopant radii in Cm³⁺-doped LaPO₄ could explain the larger DW factor than obtained for Cm³⁺ incorporation in GdPO₄. The large DW factor obtained for La_{0.5}Gd_{0.5}PO₄ in comparison to the monazite end-members is in concordance with the excitation line broadening observed for the monazite solid solutions in the Cm³⁺ excitation spectra (see final report of 02NUK021CX), implying an increasing disordering of the monazite crystal structure.

Further details of the monazite local structure could be derived only for the LaPO₄ sample (Table 4). The FTM of this sample shows distinct backscattering peaks assignable to Cm-P (marked in orange) and Cm-La interactions (marked in blue). With space group P 1 21/n 1(14), the monazite structure shows poor radial distribution ordering of the atoms around the cation centers. In LaPO₄, for instance, the coordination shell of nine oxygen atoms has La-O distances (R_{La-O}) ranging from 2.45 to 2.78 Å; the seven P atoms from the phosphate units directly linked to this LaO₉ polyhedron have distances ranging from 3.20 to 3.79 Å, followed by 3 La neighbors from 4.08 to 4.15 Å and another three La neighbors from 4.30 to 4.36 Å. Since the distal resolution of EXAFS is limited by $\pi/(2*\Delta\chi)$, shells have to be separated by at least 0.21 Å, given the limited k-range available (2.0 to 9.5 Å⁻¹). Therefore, the different individual interatomic distances had to be grouped into shells for EXAFS fitting. The most stable fits were obtained with the following grouping: a coordination shell of 9 oxygen atoms, 3 shorter and 4 longer cation-P distances, 3 shorter and 3 longer cation-cation distances. The results derived from the corresponding fit are shown in Table 4. The coordination shell could be fitted with 9 Cm-O paths at an average distance of 2.46 Å, hence showing the expected contraction in relation to LaPO₄ because of the smaller ionic radius of Cm³⁺ as shown above. The relatively high disorder expressed by a Debye-Waller factor of 0.90 Å² is in line with the expected distorted tricapped prism structure. The two Cm-P paths provided distances at 3.25 and 3.69 Å, in line with the LaPO₄ structure determining the long-

range order around Cm^{3+} . The following two Cm-La shells were fitted with average distances of 4.08 and 4.42 Å, again largely in line with the monazite structural model. In conclusion, the local environment of Cm is except for the coordination shell determined by the LaPO_4 structure. No clustering of Cm-centers is visible, which would be observable by the short-range probe EXAFS, but not by long-range probes like XRD as was observed for instance for metal oxides, silicates and phosphates (Ellis et al., 2006; Hazemann et al., 1992; Henderson et al., 2001; Martin et al., 2007; Scavini et al., 2012; Scheinost et al., 1999; Scheinost et al., 2001; Vantelon et al., 2003).

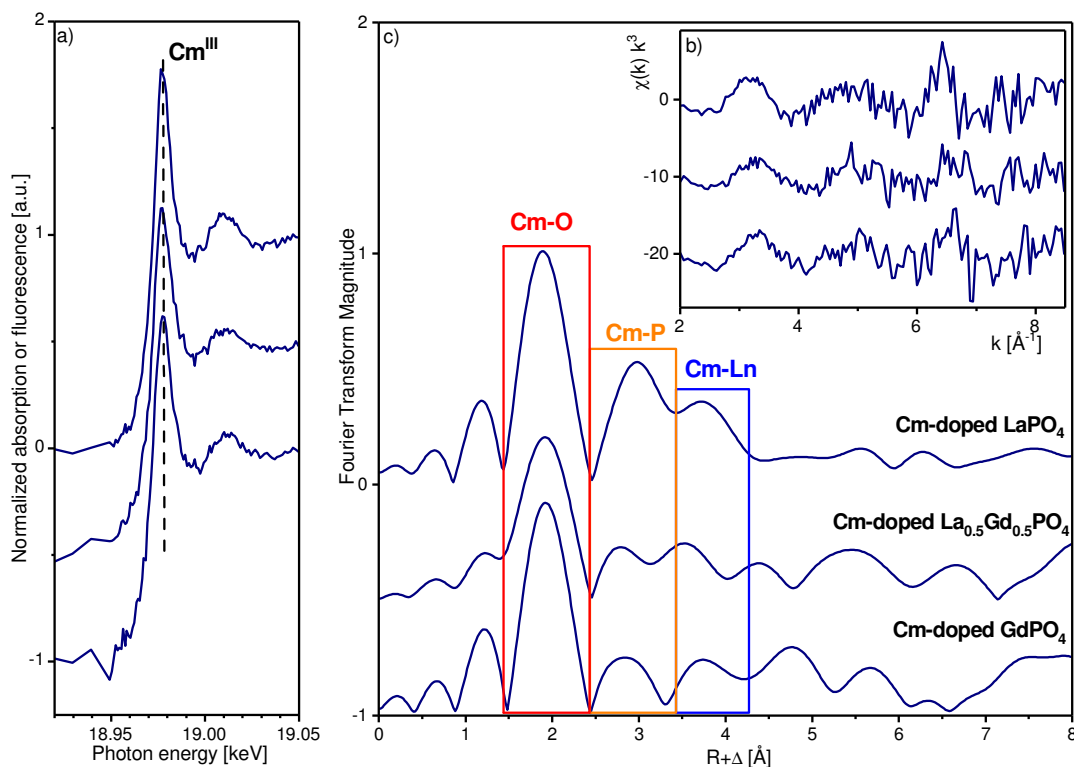


Fig. 14. Cm L_{3} -edge XAFS spectra of the Cm-doped monazites. a) XANES, b) k^3 -weighted EXAFS spectra, and c) their Fourier transform magnitude.

Table 4. Cm- L_{III} EXAFS fit results of the Cm-doped phosphate phases (fit range 1.5 – 8.5 Å⁻¹).

Sample	Path	CN	R [Å]	σ^2 [Å ²]	ΔE_0 [eV]	S_0^2	χ_{res} [%]
LaPO ₄ (Cm)	Cm-O	9	2.46	0.0090	7.3	0.80	19.2
	Cm-P	3	3.25	0.0068 ^c			
	Cm-P	4	3.69	0.0068 ^c			
	Cm-La	3	4.08	0.0030 ^c			
	Cm-La	3	4.42	0.0030 ^c			
La _{0.5} Gd _{0.5} PO ₄ (Cm)	Pu-O	9	2.43	0.0120	8.8	0.57	12.6
GdPO ₄ (Cm)	Pu-O	9	2.43	0.0063	8.8	0.50	16.5

CN: coordination number, R: radial distance, σ^2 : Debye-Waller term, ΔE_0 : phase shift, S_0^2 : amplitude reduction factor, χ_{res} : residual error, c: parameters were correlated during the EXAFS fit

In summary, the XAFS investigation in line with the laser-spectroscopic results of the Cm^{3+} -doped monazites confirm the results obtained for Eu^{3+} . The results clearly indicate that Cm^{3+} is substituted for the host cation sites in all investigated monazites. Although the spectroscopic data

suggest a disordering of the monazite solid solution series due to less explicit Ln···O bond distances in the mixed solids, the spectroscopic investigations also imply that no preferential incorporation of dopants on host cation sites with similarly sized cation radii occurs, which is of great importance when considering the performance of monazite materials as immobilization matrices for highly radioactive actinide compounds (Huittinen et al., in preparation).

This work has been performed in close collaboration with 02NUK021C and has been used to prepare the following article:

Huittinen, N., Scheinost, A.C., Wilden, A., Arinicheva, Y. and Stumpf, T. (in preparation) A spectroscopic study on Cm³⁺ incorporation in lanthanide phosphate rhabdophane (LnPO₄·nH₂O) and monazite (LnPO₄).

2.1.5 Incorporation of thorium in thorite–xenotime solid solutions

The mineral xenotime hosting the heavy lanthanides has a zircon-type structure in common with phosphates and silicates of tetravalent actinides, including ThSiO₄ (thorite), USiO₄ (coffinite) and their solid solutions (Clavier et al., 2014). They all crystallize in the tetragonal system with space group I4₁/amd. Silicate-based compounds of this family also include zircon (ZrSiO₄) and hafnion (HfSiO₄). Although both xenotime and zircon compounds are crystallizing in the same structure type, there is no study dedicated to the existence of a solid solution between both end-members. In this present paper, we report the first synthesis of a complete solid solution of Th_{1-x}Er_x(SiO₄)_{1-x}(PO₄)_x (with 0 ≤ x ≤ 1) in the thorite–xenotime system. Thorium was selected as a model element for tetravalent actinides thereby avoiding perturbations due to redox reactions. All of the compounds prepared were thoroughly characterized from a structural point of view by PXRD and EXAFS. Vibrational spectroscopy features were also investigated by Raman and FTIR.

EXAFS measurements were performed in transmission mode at the Th L₃-edge (16 300 eV) and the Er L₃-edge (8358 eV) of Th_{1-x}Er_x(SiO₄)_{1-x}(PO₄)_x samples mixed with boron nitride (BN). The measurements were carried out at The Rossendorf Beamline (BM20) dedicated to actinide-based compounds, located at the European Synchrotron Radiation Facility (ESRF; Grenoble, France). The storage ring operated at 6 GeV and 170–200 mA. For the Th L₃-edge, a double Si(111) 30° crystal monochromator was used for energy selection, and a pair of Rh mirrors was used for vertical beam collimation and suppression of higher-order harmonics. A gas mixture of 80% N₂ and 20% Ar was used in the 30 cm ionization chamber measuring the incoming beam (I0), and 100% Ar gas was used to measure the beam transmitted through the sample (I1) and after the respective reference foil (I2), all filled at ambient pressure. For the Er L₃-edge, a double Si(111) 0° crystal monochromator was used for energy selection combined with a pair of Si/Rh mirrors. A gas mixture of 70% He and 30% N₂ was used in I0. Energy calibration was done by measuring the absorption spectra of Y (17 038 eV) and Ni (8333 eV) metal foils placed between I1 and I2 parallel to the sample scans. All the samples were measured at room temperature. Data reduction and extraction of EXAFS oscillation was performed using the Athena and Artemis package (Ravel and Newville, 2005). The threshold energy, E₀, was defined as the maximum of the first derivative of the absorption coefficient. Experimental EXAFS spectra were Fourier transformed using a Hanning window over the k-space ranges 2–11 Å⁻¹ for thorium and 2.5–11 Å⁻¹ for erbium. The shell fits were performed in R-space using k¹-, k²-, and k³-weighting for thorium and erbium. Theoretical phase shifts and backscattering amplitudes were obtained with the ab initio code FEFF8.2 (Ankudinov and Rehr, 1997) using the ThSiO₄ (thorite) (Taylor and Ewing, 1978) and ErPO₄ (xenotime) structures (Ni et al., 1995) for thorium and erbium L₃-edges. The calculation was carried out with a cluster of 6 Å in radius, taking into account all single scattering (SS) and multiple scattering (MS) paths. During the fitting procedure, Th–O, Th···Si1 (P2), Th···Si2 (P2), and Th–Th (Er) single scattering paths (SS) were taken into account. Similarly, Er–O, Er···P1 (Si1), Er···P2 (Si2), and Er–Er (Th) SS were considered for the fitting. The distance (R) and Debye–Waller (DW) factor were treated as free parameters, while the coordination number (N) was constrained at crystallographic values. A single shift in the threshold energy (ΔE₀) for each composition was varied as a global parameter. The amplitude reduction factor S₀² was obtained for ThSiO₄ and for ErPO₄ after keeping the obtained value constant through the whole

composition range. To ensure transferability of phase and amplitude and to allow the estimation of systematic errors, all the data were analyzed using the same experimental phases and amplitude, filtering procedures and parameters in a similar way.

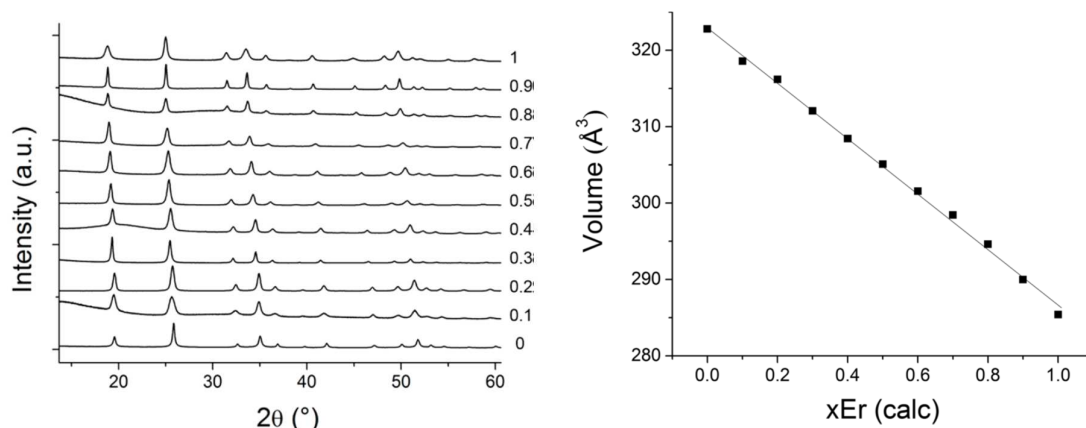


Fig. 15. PXR D of the $\text{Th}_{1-x}\text{Er}_x(\text{SiO}_4)_{1-x}(\text{PO}_4)_x$ solid solutions sorted along decreasing erbium fraction (left) and unit-cell volume showing a strictly Vegard-like decrease with increasing erbium fraction (right).

PXR D showed that all samples were monocrystalline with the expected zircon-type structure, which a decreasing unit cell volume with increasing Er substitution strictly following Vegard’s law (Fig. 15) and in line with the ionic radii of Th^{4+} (1.19 Å) and Er^{3+} (1.144 Å) in eight-fold coordination (Shannon and Prewitt, 1969). From the long-range order point of view, therefore, the solid solution forms a perfectly random distribution of Th/Er and of Si/P at the respective crystallographic sites. In order to investigate, if this is also true for the short range order, we performed EXAFS measurements at both the Th L_3 and the Er L_3 edges (Fig. 16).

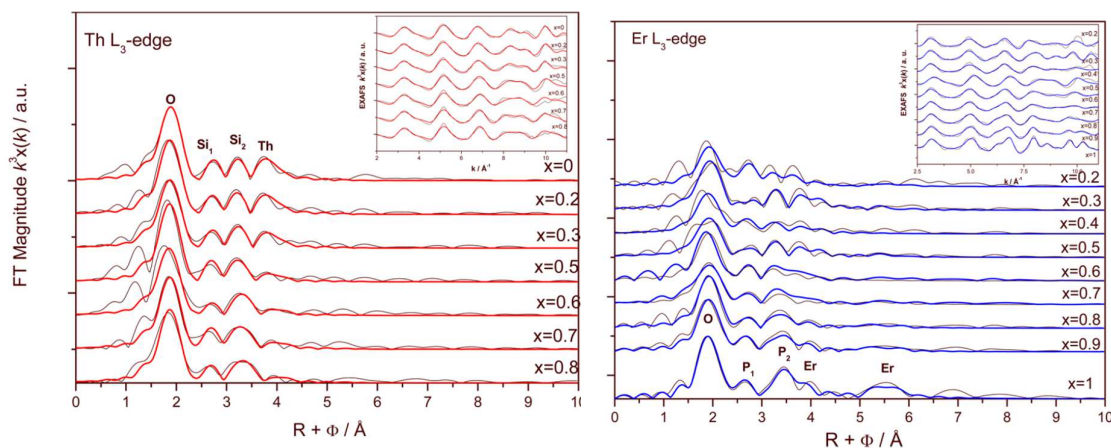


Fig. 16. Experimental $k^3\chi(k)$ EXAFS spectra of $\text{Th}_{1-x}\text{Er}_x(\text{SiO}_4)_{1-x}(\text{PO}_4)_x$ solid solutions and their respective Fourier transforms (FTs) at the (left) Th L_3 -edge and (right) Er L_3 -edge. Colored lines are the best fit achieved; black lines are the experimental data. FT peak positions are not corrected for phase shifts.

The FT obtained for the ThSiO_4 end-member ($x = 0$) at the Th L_3 -edge shows a first shell around the thorium atom consisting of eight oxygen contributions at 2.4 Å. The next neighbor contributions at 3.20 and 3.95 Å were assigned to the single scattering contributions of two Si_1 and four Si_2 atoms in the thorite structure, respectively. Additionally, a cation–cation scattering path related to Th–Th was fitted at 3.93 Å. Besides, the FT determined for ErPO_4 ($x = 1$) at the Er L_3 -edge (Fig. 16 right) also shows the eight oxygen contributions in the first coordination shell at 2.34 Å. In the same way as that for ThSiO_4 , the FT of ErPO_4 presents a second and a third peak related to the single scattering contribution of two

P₁ at 3.03 Å and four P₂ at 3.88 Å. For the ErPO₄ end-member, it was also possible to fit two Er–Er distances, at 3.76 and 5.69 Å. The fit values are compiled in

Table 5 and were found to be in agreement with the average crystal diffraction distances reported in the literature (Ni et al., 1995; Taylor and Ewing, 1978). For intermediate solid solutions, the FT measurements at the Th L₃-edge from x = 0 to x = 0.5 showed little changes on the local environment around Th. However, starting from x = 0.5 to x = 0.8, the amplitude of Th peak contribution decreased and the Si₂ peaks broadened. Such behavior might be related to the shortening of Th–Th(Er) distances as the actinide content decreased and/or to interferences between the two Er and Th scattering paths resulting in the attenuation of the cation–cation FT peak. The EXAFS spectra for the Th L₃-edge showed no modification at lower k-ranges. However, small modifications started at 8 Å⁻¹, which is probably due to the mixing backscattering between Th and Si atoms. Conversely, the FTs at the Er L₃-edge showed more significant changes in the local environment around Er than those of the Th L₃-edge at higher Er content (x = 0.9). Such modifications were also revealed in their EXAFS spectra, where a more substantial change in the atomic structure around the xenotime ErPO₄ was observed as Th content increased.

Table 5. EXAFS shell fit results for the Th (top) and Er local structure (bottom) of Th_{1-x}Er_x(SiO₄)_{1-x}(PO₄)_x

x	Th–O		Th–Si ₁		Th–Si ₂		Th–Th		S ₀ ² = 0.81 % R-factor = 2.0 E ₀ = 10.88
	R/Å	σ ² /Å ²	R/Å	σ ² /Å ²	R/Å	σ ² /Å ²	R/Å	σ ² /Å ²	
0	2.40 (8)	0.0058 (13)	3.20 (25)	0.0045 (36)	3.95 (36)	0.0077 (51)	3.93 (16)	0.0042 (18)	
0.2	2.39 (6)	0.0057 (7)	3.18 (22)	0.0046 (29)	3.95 (26)	0.0061 (35)	3.92 (14)	0.0044 (15)	% R-factor = 1.1 E ₀ = 10.16
0.3	2.40 (5)	0.0067 (8)	3.19 (25)	0.0050 (33)	3.95 (24)	0.0050 (32)	3.93 (17)	0.0056 (19)	% R-factor = 1.4 E ₀ = 10.37
0.4	2.38 (7)	0.0049 (11)	3.19 (71)	0.0102 (12)	3.92 (39)	0.0045 (53)	3.90 (40)	0.0078 (50)	% R-factor = 2.8 E ₀ = 10.37
0.5	2.38 (9)	0.0053 (8)	3.16 (26)	0.0033 (36)	3.93 (29)	0.0036 (37)	3.91 (37)	0.0084 (45)	% R-factor = 2.2 E ₀ = 9.75
0.6	2.38 (9)	0.0069 (11)	3.17 (50)	0.0084 (80)	3.94 (25)	0.0018 (30)	3.90 (43)	0.0085 (45)	% R-factor = 2.9 E ₀ = 9.75
0.7	2.39 (10)	0.0062 (11)	3.16 (22)	0.0022 (30)	3.95 (23)	0.0014 (27)	3.92 (35)	0.0080 (43)	% R-factor = 2.5 E ₀ = 10.49
0.8	2.39 (9)	0.0060 (10)	3.16 (27)	0.0039 (39)	3.95 (21)	0.0010 (24)	3.90 (33)	0.0074 (39)	% R-factor = 2.1 E ₀ = 10.47
x	Er–O		Er–P ₁		Er–P ₂		Er–Er		S ₀ ² = 0.77 % R-factor = 4.4 E ₀ = 15.47
	R/Å	σ ² /Å ²	R/Å	σ ² /Å ²	R/Å	σ ² /Å ²	R/Å	σ ² /Å ²	
0									
0.2	2.38 (14)	0.0111 (16)	3.08	0.0012	3.88	0.0101	3.94 (54)	0.0101	% R-factor = 4.4 E ₀ = 15.47
0.3	2.36 (9)	0.0078 (10)	3.05 (29)	0.0073 (43)	3.83 (23)	0.0041 (14)	3.98 (16)	0.0041 (14)	% R-factor = 2.5 E ₀ = 14.69
0.4	2.35 (10)	0.0105 (12)	3.05 (25)	0.0040 (26)	3.84 (38)	0.0084 (38)	3.98 (40)	0.0084 (38)	% R-factor = 4.1 E ₀ = 14.28
0.5	2.36 (10)	0.0108 (14)	3.05 (33)	0.0088 (58)	3.83 (30)	0.0066 (23)	3.97 (24)	0.0066 (23)	% R-factor = 3.5 E ₀ = 14.77
0.6	2.35 (10)	0.0086 (11)	3.06 (22)	0.0047 (35)	3.83 (42)	0.0102 (45)	3.96 (42)	0.0102 (45)	% R-factor = 3.2 E ₀ = 14.40
0.7	2.36 (8)	0.0100 (10)	3.06 (22)	0.0067 (30)	3.85 (35)	0.0110 (36)	3.95 (34)	0.0110 (36)	% R-factor = 2.3 E ₀ = 15.00
0.8	2.35 (7)	0.0074 (9)	3.05 (24)	0.0070 (38)	3.89 (63)	0.0100 (35)	3.78 (62)	0.0100 (35)	% R-factor = 2.2 E ₀ = 14.74
0.9	2.35 (8)	0.0073 (9)	3.04 (18)	0.0036 (25)	3.89 (51)	0.0096 (26)	3.77 (53)	0.0096 (51)	% R-factor = 2.3 E ₀ = 15.02
1.0	2.34 (7)	0.0055 (8)	3.03 (16)	0.0018 (19)	3.88 (34)	0.0049 (11)	3.76 (22)	0.0049 (11)	% R-factor = 2.3 E ₀ = 14.97

According to the criteria for isovalent solid solutions, the bond length could be limited by two cases, which will reflect their ability to adapt to the host structure. The first is *no relaxation* in the system, which assumes that the atomic radii are approximately conserved and independent of the composition

of the solid solution (Pauling's concept). In contrast, the second corresponds to *full relaxation* in the system, where the virtual crystal approximation (VCA) is valid and bond lengths follow Vegard's law (Martins and Zunger, 1984). The cation–oxygen interatomic distances are presented in Fig. 17, with respective error bars calculated from the difference of EXAFS values and the distances of the crystal structure. The derived Th–O and Er–O bond length distances showed that Th–O and Er–O distances are element-specific due to the difference in their crystal effective radius given before. The Er–O bond length determined by EXAFS increased in the zircon-type structure with the thorium content. However, the individual Th–O bond length remained close to the value determined in pure ThSiO_4 (2.39 Å); i.e., there is no relaxation. It suggests that Th–O bond lengths are preserved in the first coordination shell as erbium content increases, due to its strong covalent bond. From these results, the host zircon-type structure (ErPO_4) is modified with the change in the actinide content (i.e., full relaxation). Besides, the average EXAFS distance plotted in Fig. 17 showed a similar trend compared to the PXRD results (Fig. 15 right). Another observation is that the Debye–Waller factor (σ^2) in the Er–O coordination shell is increasing with thorium content, from 0.0050 to 0.0100 Å², while the σ^2 values for the Th–O contribution remained at an average of 0.006 Å². Note that the Debye-Waller factors given in

Table 5 reflect both thermal and static contributions since the EXAFS measurements were performed at room temperature.

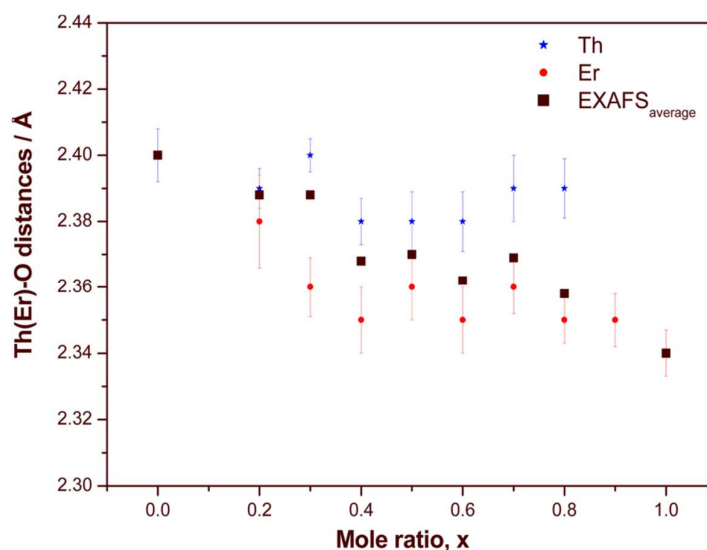


Fig. 17. Interatomic distances Th–O (upper ■) and Er–O (bottom ★) vs composition in $\text{Th}_{1-x}\text{Er}_x(\text{SiO}_4)_{1-x}(\text{PO}_4)_x$ solid solutions. The square symbols represents the average value obtained by EXAFS.

The cation–cation distribution is given by a single broad FT peak not resolving several distances present in the structure. The variation in the second neighbor distribution is presented in Fig. 18 with the corresponding error bars. First, the Er–Er (Th) and Th–Th (Er) distances are approximately equal to their average distances, as reported previously in the case of covalent and ionic systems. Second, with a look at the Er–Er (Th) local environment, a change from 3.76 to 3.94 Å was observed. Nonetheless, the Th–Th (Er) local environment suffered a small variation from 3.93 to 3.90 Å. These results again suggest that although the Er local structure was modified, that of Th remained close to that of pure thorite (ThSiO_4). This kind of behavior was already reported for stabilized zirconia with actinides (Nastren et al., 2009; Walter et al., 2011). In addition, as the thorium content increased, the Er–Er (Th) bond length distances became similar to the Th–Th ones. Finally, Fig. 19 shows the variation in the Er–P and Th–Si interatomic distances. It is important to mention that P and Si are undistinguishable by EXAFS because of their close atomic number. However, from fitting, it was observed that Th–Si and Er–P distances remained almost constant, meaning that there is a less significant change in their distances than those obtained for the cations.

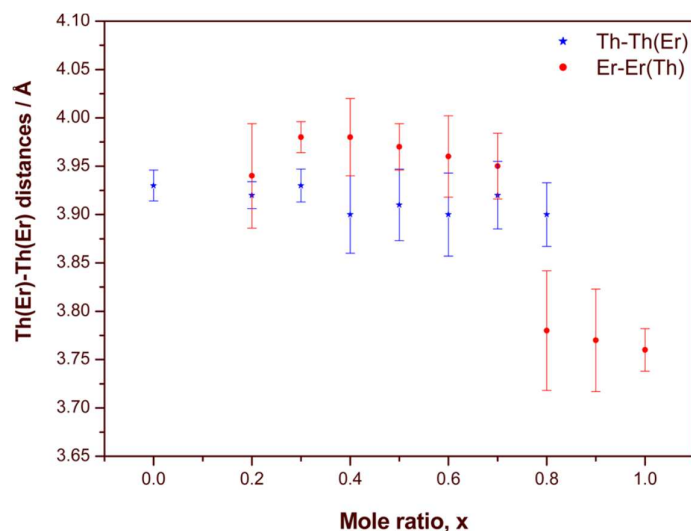


Fig. 18. Variation in the interatomic distances Th-Th(Er) (★) and Er-Er(Th) (●) vs composition in $Th_{1-x}Er_x(SiO_4)_{1-x}(PO_4)_x$ solid solutions.

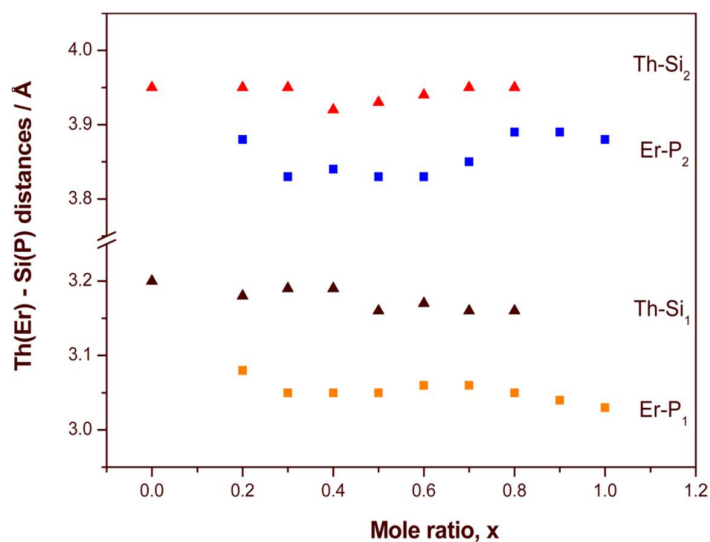


Fig. 19. Variation in the interatomic distances Th(Er)-Si(P) vs. composition in $Th_{1-x}Er_x(SiO_4)_{1-x}(PO_4)_x$ solid solutions.

Therefore, our results confirm the formation of a complete solid solution over the whole composition range. In agreement with Vegard's law, the crystal structure of these solids exhibited a linear decrease of the unit cell volume as a function of the erbium/phosphate content. However, the analysis of the local structure with EXAFS measurements shows that the Th-O distances do not evolve so much during the erbium to thorium substitution and remain close to those found for the thorite end-member ($ThSiO_4$). On the contrary, the Er-O-(P,Si) sequence suffers more than Th-O-(P,Si) during the (Th, SiO_4) \leftrightarrow (Er, PO_4) substitution, by showing a large increase of the Er-O distance when increasing the thorium content in the structure. Correspondingly, a distortion of the phosphate groups was observed by spectroscopy.

This work has been performed in cooperation with Institut de Chimie Séparative de Marcoule (ICSM), Marcoule, France, and has been published (Mesbah et al., 2016).

2.1.6 The local structure of Sm and Tb in $\text{Sm}_{1-x}\text{Tb}_x\text{PO}_4$: Monazite to xenotime transition

Among the phosphates considered as waste forms for long-lived radionuclides, monazite stands out because of its low solubility, slow dissolution rate and high chemical flexibility to incorporate actinide elements such as Am and Cm. EXAFS was carried out to evaluate the local structure of the $\text{Sm}_{1-x}\text{Tb}_x\text{PO}_4$ solid-solution between the Sm endmember with monazite and the Tb endmember with xenotime structure. To this end, solid solutions of $\text{Sm}_{1-x}\text{Tb}_x\text{PO}_4$ with $x = 0 - 1$ were synthesized using wet-chemical precipitation at room temperature similar to (Boakye et al., 2008). EXAFS measurements were carried out at ROBL (ESRF, Grenoble). Spectra were collected at the Sm L_3 (6716 eV) and Tb L_3 (7514 eV) edges, using a He cryostat (15 K), in fluorescence or transmission mode depending on concentration. The experimental spectra were Fourier-transformed using a Hanning window across $2.0 - 9.0 \text{ \AA}^{-1}$ for Tb and Sm. Monazite and xenotime models as reported earlier (Ni et al., 1995) were used for the data refinement, which was done with WinXAS (Ressler, 1998).

Powder diffraction shows that the samples up to $x=0.65$ consist predominately of monazite, while the sample at $x=0.8$ is already predominated by the xenotime structure, fully obtained for the Tb phosphate endmember (Fig. 20). Fig. 21 shows the Sm- L_3 edge spectra of the $\text{Sm}_{1-x}\text{Tb}_x\text{PO}_4$ solid solution samples up to $x=0.80$, and for comparison the Tb- L_3 edge spectrum of $x=1.00$. The samples from $x=0$ to $x=0.75$ show little changes of the local environment around Sm. Only for $x=0.8$ the spectrum changes significantly and becomes more similar to the spectrum of pure TbPO_4 with xenotime structure shown on the bottom. In a first step, the spectra were analyzed by ITFA (Iterative Transformation Factor Analysis) (Rossberg et al., 2003). All seven Sm- L_3 edge spectra including the Tb- L_3 edge spectrum could be reconstructed by two principal components (red lines in Fig. 21), demonstrating that only two different local environments around the Sm(Tb) centers are present, corresponding to the cation centers in monazite and xenotime. Using the spectra of $x=0.00$ and $x=1.00$ as pure endmembers, the fractions of these two endmembers in the solid solution series could be determined with iterative target test (Table 6). In confirmation of the visual observation, the local structure is up to $x=0.75$ dominated by monazite, while $x=0.80$ is a 50/50 mix of both monazite and xenotime local structures.

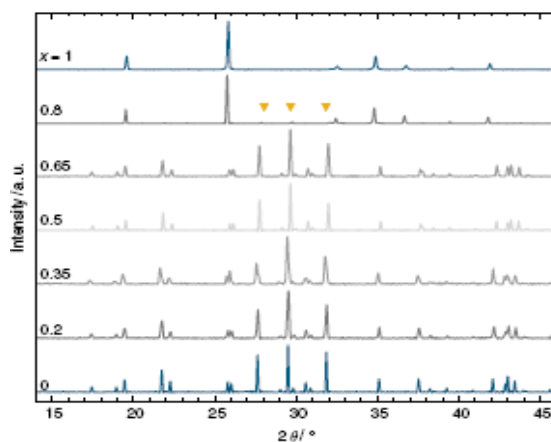


Fig. 20. PXRD of Sm/Tb phosphate solid solutions.

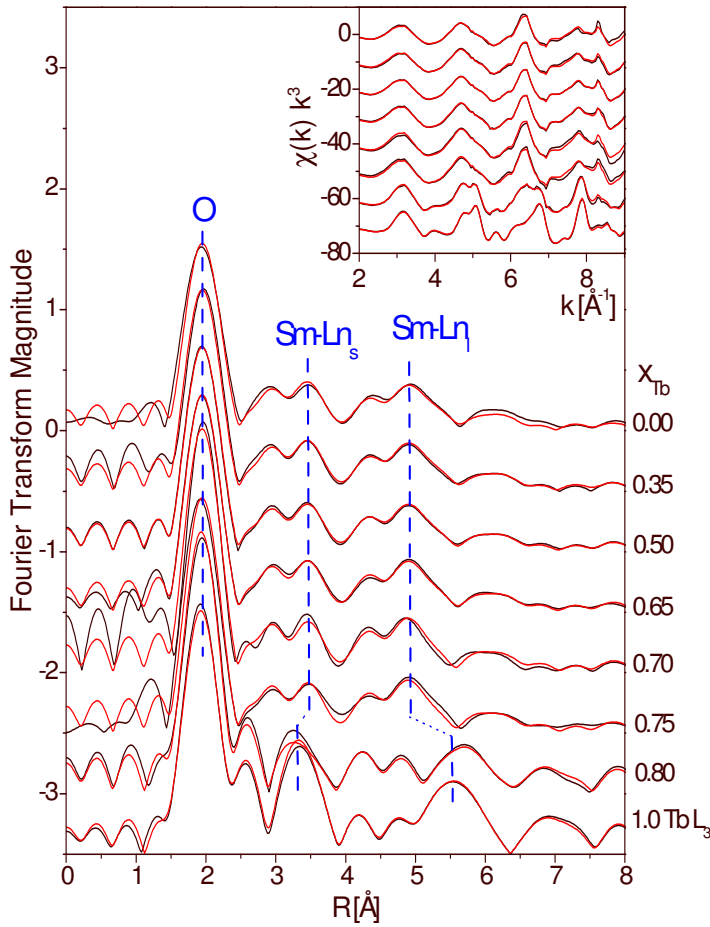


Fig. 21. Sm-L₃ edge EXAFS spectra for the Sm_{1-x}Tb_xPO₄ solid solutions up to x=0.8, compared to the Tb-L₃ edge spectrum for x=1.00 (Fourier transform magnitude; k³-weighted EXAFS as insert). Black lines are the experimental spectra, red lines their reconstruction with two principal components.

Table 6. Fraction of monazite and xenotime determined by ITFA.

x	Monazite	Xenotime
0.00	1.00	0.00
0.35	0.99	0.01
0.50	0.96	0.04
0.65	0.96	0.04
0.70	0.92	0.08
0.75	0.93	0.07
0.80	0.44	0.56
1.00	0.00	1.00

In a second step, the spectra were analyzed by shell fit. Up to x=0.75, the spectra can be fit with the monazite model, while for x>0.75, the xenotime model had to be used (Ni et al., 1995). The Sm-O bond length remains unchanged up to x=0.65 at 2.34 Å corresponding to 9-coordinated monazite, and then decreases with x linearly to the bond length of 8-coordinated xenotime, i.e. 2.37 Å (Fig. 22). For the nearest and next-nearest Sm/Tb neighbors (note that Sm and Tb backscattering functions cannot be distinguished by EXAFS), the distances remain unchanged up to x=0.75 at the values of monazite, and then change abruptly to the distances of xenotime.

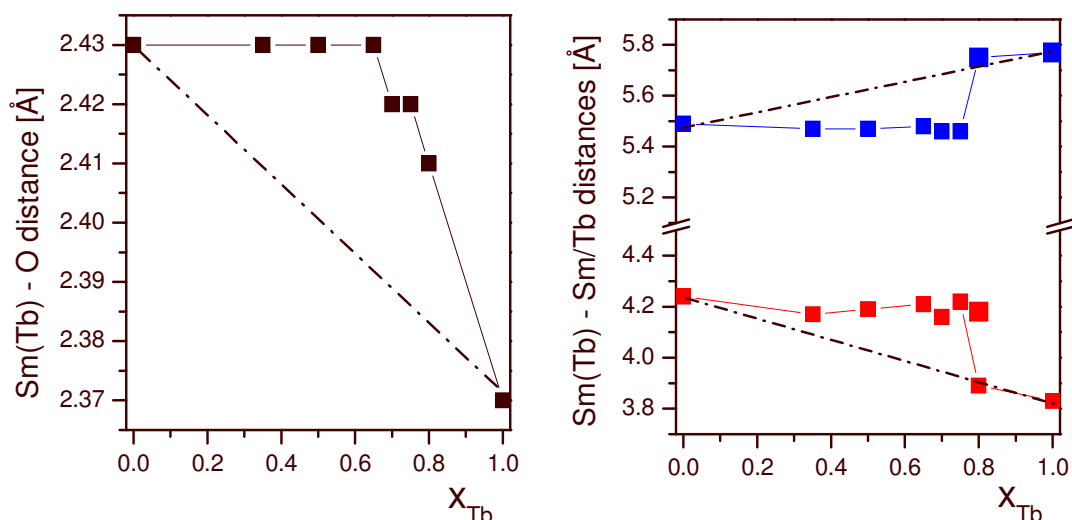


Fig. 22. EXAFS shell fit-determined distances between Sm(Tb) and O (left side) and between Sm(Tb) and nearest and next-nearest (Sm/Tb) neighbors (right side) of the $Sm_{1-x}Tb_xPO_4$ series as a function of x .

The high flexibility of the monazite structure to host foreign cations is hence due to the fact, that monazite remains the dominant phase up to $x=0.75$. Only at $x=0.8$, the Sm local environment changes to the xenotime local structure in a rather abrupt step. Our results hence provide the crystal chemical cause for the ability of monazite to host a very high percentage of foreign cations, which makes it such a promising candidate for the safe enclosure of long-lived actinides.

This work has been performed in close cooperation with FZJ-IEK6 (O2NUK021A). A manuscript is in preparation.

2.1.7 The local structure of La/Eu/Lu phosphate: Monazite to xenotime transition

The series $La_{0.7-x}Eu_{0.3}Lu_xPO_4$ was investigated by EXAFS spectroscopy to shed light on the local structure around the early lanthanides La and Eu and around the heavy Lu with increasing Lu fraction x . The samples were prepared by precipitation molar ratios of $(0.7-x) La(NO_3)_3 + 0.3 Eu(NO_3)_3 + x Lu(NO_3)_3$ followed by washing steps with HNO_3 and deionised water to remove soluble salts and amorphous solids, and then pellets were sintered at $1400^\circ C$. The long-range structure at $x=0.2$ is dominated by the monazite structure expected for the predominance of the lighter lanthanides La and Eu, which is also shown for the complete La-Eu phosphate solid-solution series (Arinicheva et al., 2014), but shows already a small contribution from xenotime (Fig. 23). This xenotime contribution increases for $x=0.35$ and 0.50 , while xenotime becomes the sole phase for $x=0.7$.

Selected samples of this series were investigated by La L_1 -edge, Eu L_3 -edge, and Lu L_3 -edge EXAFS spectroscopy to probe the local structure around La, Eu and Lu cationic centers (Fig. 24). As a comparison with the spectrum of the $LuPO_4$ endmember shows, remains the local environment around Lu xenotime-like for $x=0.35$ and higher, and becomes monazite-like only for $x=0.2$. This latter result is somewhat surprising given the fact, that the PXRD pattern shows already at this low x a small contribution from xenotime. As the comparison with the spectrum of the pure $EuPO_4$ endmember shows, is the local environment around Eu monazite-like up to $x=0.5$, and becomes xenotime-like only for $x=0.7$. La spectra were only available for x up to 0.35 , but also show only a monazite-like local structure. Therefore, the prevalence of xenotime for $x=0.7$ at the long range structure level is maintained also for Eu and Lu at the local structural level.

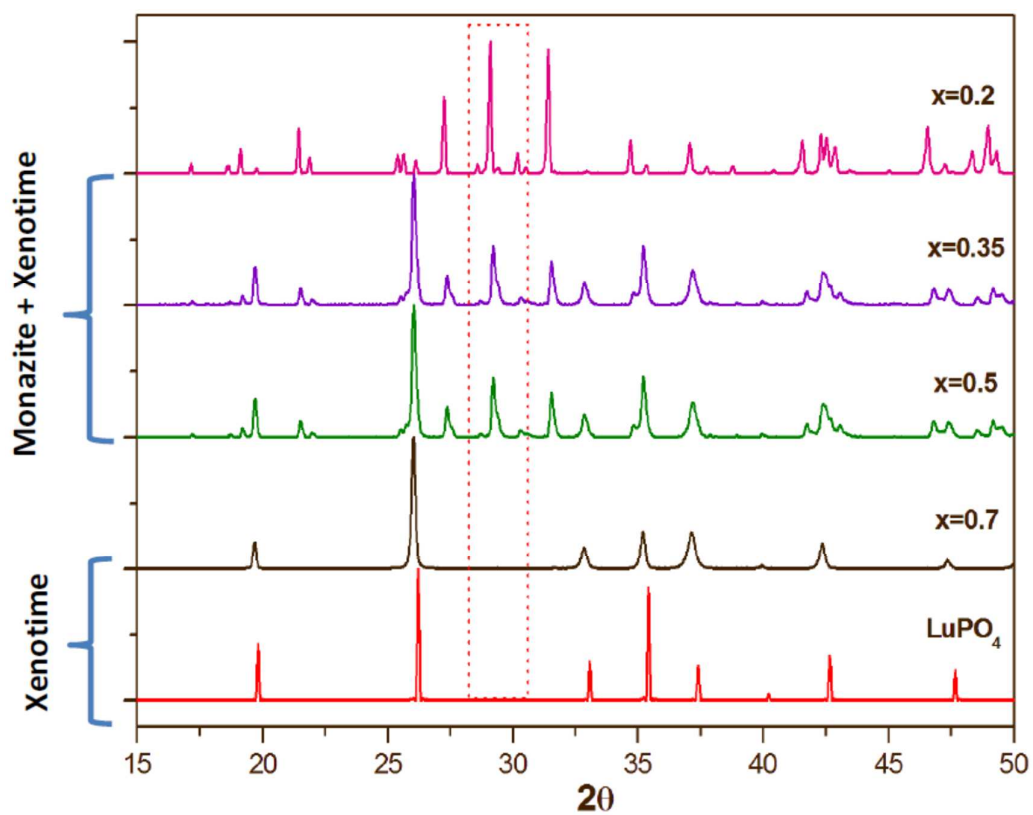


Fig. 23. PXR D patterns of the $La_{0.7-x}Eu_{0.3}Lu_xPO_4$ solid solution series.

The experimental spectra were fitted making use of clusters based on the crystallographic structures of monazite and xenotime as detailed before, using, Ln-O, two Ln-P, and two Ln-Ln single scattering paths. Fig. 7 shows some of these paths. Note that the short Ln-Ln path interferes with the two Ln-P paths at the same position, resulting in relatively high errors for the fit parameters of these relatively weak Ln-P scattering pairs.

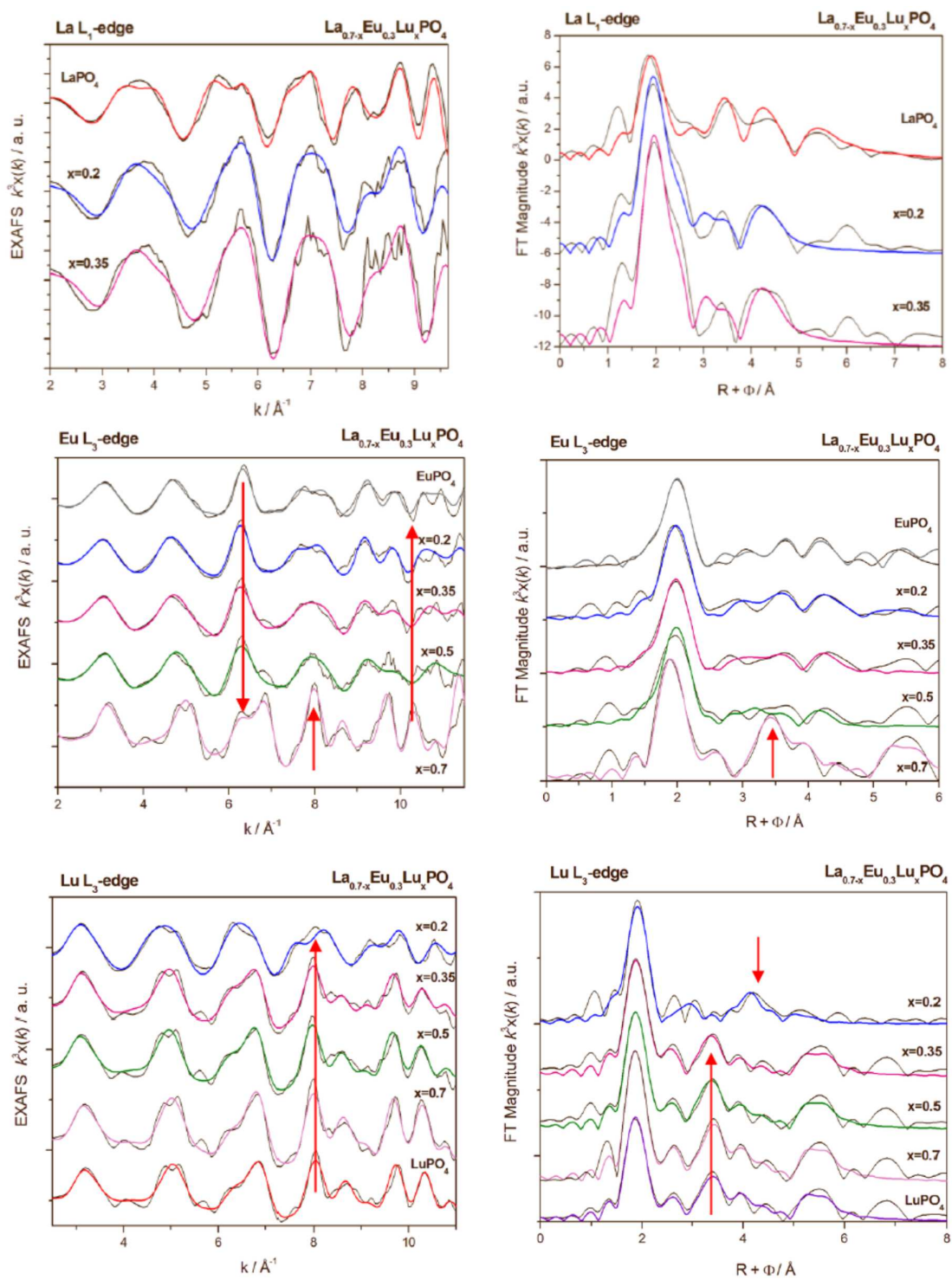


Fig. 24. La L_1 -edge, Eu L_3 -edge, and Lu L_3 -edge EXAFS spectra of $\text{La}_{0.7-x}\text{Eu}_{0.3}\text{Lu}_x\text{PO}_4$ solid solutions along with pure endmembers. Left: k^3 -weighted EXAFS spectra, right: the corresponding Fourier transform magnitudes.

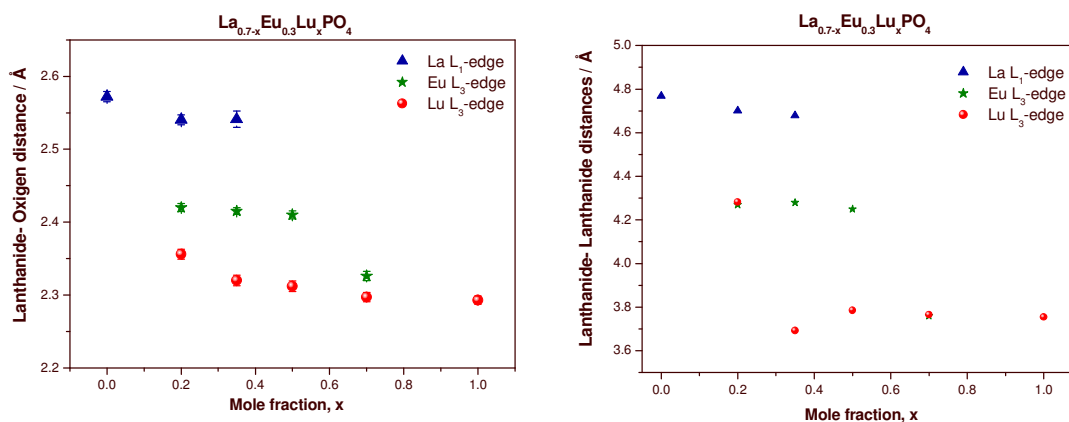


Fig. 25. Ln-O and Ln-Ln distances in the $\text{La}_{0.7-x}\text{Eu}_{0.3}\text{Lu}_x\text{PO}_4$ series determined by shell fits of La-L₁, Eu-L₃ and Lu-L₃ edge EXAFS spectra.

Table 7. EXAFS fit results of the $\text{La}_{0.7-x}\text{Eu}_{0.3}\text{Lu}_x\text{PO}_4$ series measured at La-L₁, Eu-L₃ and Lu-L₃ edges.

Lu L ₃ -edge									
x	Lu-O		Lu-P1		Lu-P2		Lu-Ln		
	R/Å	σ ² /Å ²	R/Å	σ ² /Å ²	R/Å	σ ² /Å ²	R/Å	σ ² /Å ²	
0									
0.2	2.36	0.0055	2.66	0.0080	3.58	0.0110	4.28	0.0059	
0.35	2.32	0.0048	3.00	0.0016	3.83	0.0016	3.69	0.0126	
0.5	2.31	0.0041	2.99	0.0016	3.80	0.0016	3.79	0.0054	
0.7	2.30	0.0033	2.99	0.0016	3.81	0.0016	3.77	0.0035	
1.0	2.30	0.0026	2.98	0.0016	3.80	0.0016	3.75	0.0043	

Eu L ₃ -edge									
	Eu-O		Eu-P1		Eu-P2		Eu-Ln		
	R/Å	σ ² /Å ²	R/Å	σ ² /Å ²	R/Å	σ ² /Å ²	R/Å	σ ² /Å ²	
0									
0.2	2.42	0.0048	2.72	0.0072	3.68	0.0048	4.27	0.0038	
0.35	2.42	0.0047	2.70	0.0099	3.69	0.0068	4.28	0.0070	
0.5	2.41	0.0054	2.65	0.0084	3.71	0.0083	4.25	0.0114	
0.7	2.33	0.0065	3.00	0.0016	3.81	0.0016	3.76	0.0018	

La L ₁ -edge									
	La-O		La-P1		La-P2		La-Ln		
	R/Å	σ ² /Å ²	R/Å	σ ² /Å ²	R/Å	σ ² /Å ²	R/Å	σ ² /Å ²	
0	2.54	0.0031	3.24	0.0027	3.81	0.0027	4.70	0.0050	
0.2	2.54	0.0031	3.25	0.0075	3.79	0.0075	4.70	0.0038	
0.35	2.54	0.0013	3.24	0.0061	3.80	0.0061	4.68	0.0025	

These results are largely confirmed by the fitted Ln-O and Ln-Ln distances (Fig. 25 and Table 7). These remain largely at the values of the pure endmembers, and deviate from this mostly for Lu-Ln at x=0.2, and for Eu-Ln at x=0.7. The corresponding Lu-O and Eu-O distances follow these two deviations, but much more buffered, demonstrating that the constraint imposed by the cation diameters cannot be fully overcome in the solid solution.

In conclusion, $\text{La}_{0.7-x}\text{Eu}_{0.3}\text{Lu}_x\text{PO}_4$ crystallizes as monazite phase for low x , and as xenotime for higher x . Lanthanum as early lanthanide, and Lu as late lanthanide, reside largely in their respective monazite and xenotime sites, and deviate only for the most extreme x investigated. Europium located in the middle of the lanthanide series, which forms a monazite-type phosphate when pure, shows a transitional behavior in the investigated solid solution. Therefore, the $\text{La}_{0.7-x}\text{Eu}_{0.3}\text{Lu}_x\text{PO}_4$ mixed phosphate solid solution shows a high flexibility going from the monazite to the xenotime structure, which is relevant for a potential host phase for nuclear waste. Furthermore, X-ray absorption demonstrated its particular usefulness for elucidating the local atomic arrangement of lanthanides mixed phosphate solid solutions, getting specific information about each element measured.

This work has been performed in close cooperation with FZJ-IEK6 (O2NUK021A). A manuscript is in preparation.

2.1.8 Rhabdophane

Hydrated phosphate compounds with a general formula of $\text{LnPO}_4 \cdot n\text{H}_2\text{O}$ ($\text{Ln} = \text{La} - \text{Gd}$), namely, rhabdophane-type, are usually considered as low temperature precursors for the preparation of monazite-type compounds. The advantage of their use arises from their simple synthesis through wet chemistry routes and their easy conversion into monazite through high temperature heat treatment. Moreover, they seem to play an important role as neoformed phases during the alteration of monazites in aqueous environments in terms of controlling the actinides release from the waste matrix. Indeed, owing to their very low solubility constants, a formation of a protective rhabdophane layer on the surface of the waste matrix in aqueous environment is most likely, which can hinder a release of the leached radioactive elements significantly (de Kerdaniel et al., 2007; Oelkers and Poitrasson, 2002; Poitrasson et al., 2004).

The rhabdophane structure was assumed to be hexagonal since mid of last century (Mooney, 1948, 1950). Very recently (Mesbah et al., 2014) reinvestigated rhabdophane endmembers ($\text{Ln} = \text{La} - \text{Dy}$) with synchrotron XRD showing a monoclinic crystal structure of these compounds instead of the hexagonal structure. Moreover, a model was presented allowing for the accurate determination of the amount and the position of the water molecules. From this study, the lanthanide rhabdophanes can be described as a mixture of 8- and 9-fold coordinated lanthanides with the general chemical composition of $\text{LnPO}_4 \cdot 0.667\text{H}_2\text{O}$.

Within this project, the structure of rhabdophane solid solution series ($\text{La}_{1-x}\text{Gd}_x\text{PO}_4 \cdot 0.667\text{H}_2\text{O}$) was investigated thoroughly by several techniques (Raman, XRD, TRLFS and XAS). The XRD patterns (Fig. 26) reveal a pure rhabdophane structure for all compositions. At 15° and 20° 2θ , the most characteristic reflexes of the rhabdophane structure are evident. In contrast, the characteristic reflexes of the monazite structure at $2\theta = \sim 22^\circ$ and 27° are missing. The absence of reflex splitting clearly indicates a successful and quantitative $(\text{La}, \text{Gd})\text{PO}_4 \cdot 0.667\text{H}_2\text{O}$ solid solution formation with rhabdophane structure directly after precipitation at a remarkably low temperature of 90°C . The red line added to the XRD patterns highlight the shift of the reflections in the XRD pattern to higher 2θ values by increasing the content of the smaller Gd^{3+} ions. These results verify a simultaneous co-precipitation of La^{3+} and Gd^{3+} ions during synthesis and demonstrate the main advantage of the precipitation route over the solid-state method.

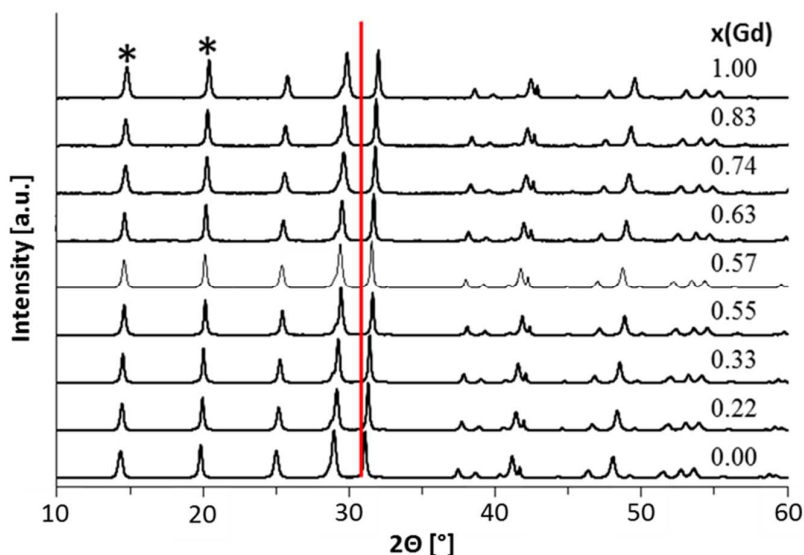


Fig. 26. Compilation of XRD patterns of $La_{1-x}Gd_xPO_4 \cdot 0.667H_2O$ solid solutions. The measurements have been performed on powders directly after co-precipitation and storage at 90 °C. The red line is added for visualization of the 2θ shift.

EXAFS measurements were performed for several samples at the Lu-L₁, the Eu-L₃ and the Gd-L₃ edges. Fig. 27 shows experimental spectra in comparison to FEFF-calculated spectra obtained for the hexagonal model of (Mooney, 1948) shown at the bottom, and the monoclinic model of (Mesbah et al., 2014). It is evident that the model of (Mesbah et al., 2014) with 1/3 of the cations in 8-fold and 2/3 of the cation in 9-fold coordination reproduces a closer match of the experimental spectra as compared to the model of (Mooney, 1948) with only 8-fold coordination of the cations. Due to the limited resolution of EXAFS, however, the shell fit could take into account only one Ln-O shell (Fig. 28, Table 8). Nevertheless demonstrates the FEFF modeling approach clearly that the short-range order is in agreement with the monoclinic model of (Mesbah et al., 2014). This was further supported by TRIFS measurements performed within O2NUK021C.

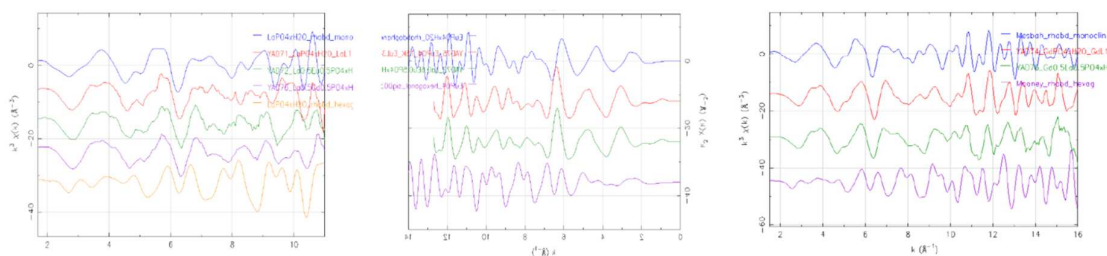


Fig. 27. EXAFS spectra of La/Eu/Gd rhabdophanes measured at the La-L₁ (left), Eu-L₃ (center) and Gd-L₃ (right) edges, in comparison to FEFF-calculated theoretical spectra based on the monoclinic model of (Mesbah et al., 2014) (top) and the hexagonal model of (Mooney, 1948) (bottom).

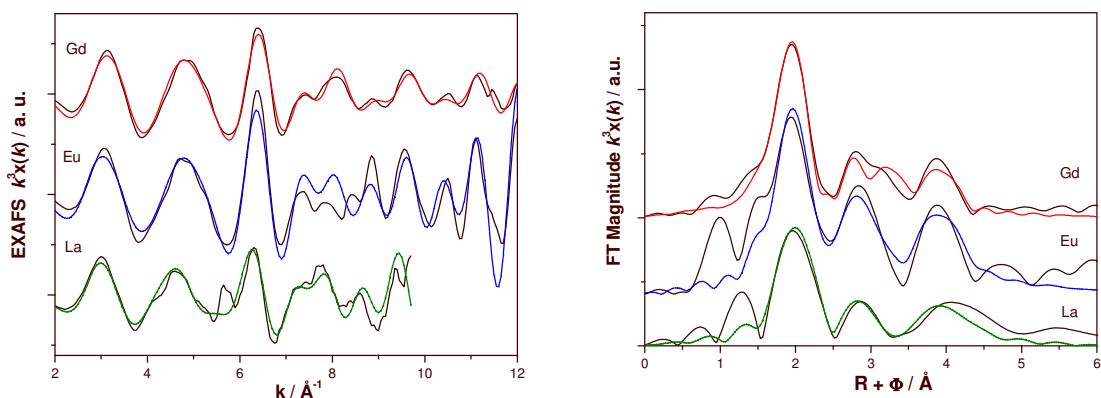


Fig. 28. Experimental (black lines) and fitted (colored lines) EXAFS spectra of a La/Eu/Gd rhabdophane sample measured at the La-L¹, Eu-L³ and Gd-L³ edges.

Table 8. Best fitting EXAFS values obtained for the La/Eu/Gd rhabdophane sample shown in Fig. 28

	La		Eu		Gd	
	R/ Å	σ^2 / Å ²	R/ Å	σ^2 / Å ²	R/ Å	σ^2 / Å ²
Ln-O	2.59 (41)	0.0036 (29)	2.40 (31)	0.0039 (27)	2.42 (25)	0.0058 (16)
Ln-P₁	3.27 (31)	0.0036 (47)	3.17 (16)	0.0020 (12)	3.17 (6)	0.0068 (16)
Ln-P₂	3.82 (58)	0.0163	3.68 (19)	0.0020 (12)	3.69 (16)	0.0068 (12)
Ln-Ln₁	4.19 (26)	0.0050 (36)	4.06 (11)	0.0025 (13)	4.06 (7)	0.0075 (11)
S ₀ ² = 0.82			S ₀ ² = 0.91		S ₀ ² = 0.86	
ΔE ₀ = 13.03			ΔE ₀ = 9.62		ΔE ₀ = 11.76	
% R-factor = 2.8			% R-factor = 2.3		% R-factor = 0.63	

This work has been performed in close cooperation with FZJ-IEK6 (02NUK021A) and HZDR (02NUK021C). A manuscript is in preparation.

2.1.9 The local structure of iodate in layered double hydroxides

¹²⁹Iodine is a long-lived radionuclide with high relevance for nuclear waste disposal, because it is weakly retained in organic-poor subsoils and rocks. This weak retention is due to the anionic species forming at oxidation states -1 (iodide, I⁻) and +5 (iodate, IO₃⁻), which are only weakly sorbed by clay minerals, while they are more strongly sorbed by Al and Fe hydroxides, but only at low pH. Layered double hydroxides (LDH) are interesting in this context, since they are naturally occurring anion exchangers, which may be able to retain both iodide and iodate. LDH form with a variety of combinations of di- and trivalent cations under circumneutral conditions, but also in contact with cement, hence are relevant for typical high- and intermediate-level radionuclide disposal settings. The purpose of the current study was to investigate the local structure of iodate taken up by several LDH phases.

EXAFS measurements were performed at the Rossendorf Beamline (ROBL) located at BM20 of the European Synchrotron Radiation Facility (ESRF) Grenoble, France, which operated the electron storage ring at 6 GeV and 130–200 mA. For this experiment, the setup was equipped with a pair of Si(111) crystals for monochromatization and a pair of Pt mirrors for vertical beam collimation. The EXAFS spectra were collected at the I K-edge (33,169 eV) in transmission mode using ionization chambers filled with 100 % Ar gas for I₀ and I₁/I₂. Energy calibration for the I K-edge was carried out by using a Sb

foil and by setting the first inflexion point of the absorption spectrum to 30,491 eV. The LDH solids 1, 3, 5, 16a, 16b, KIO_3 and the KI samples were measured at 15 K using a close-cycle helium cryostat to improve signal quality by suppressing thermal contributions to the Debye–Waller factor. Internal energy calibration was performed against potassium iodide. The EXAFSPAK program package was used for data treatment. For each sample, 1–2 scans were averaged after energy calibration by means of the EXAFSPAK program package. The experimental spectra were Fourier-transformed using the k-window over the k-space ranging between 2 and 13 \AA^{-1} for I. The theoretical phase shift and backscattering amplitudes were obtained using the known crystalline KIO_3 and KI structures. The calculated EXAFS structure parameters were refined using FEFF ver. 7.02 (Ankudinov and Rehr, 1997) based on models considering only single scattering contributions. The data were analyzed by fixing the coordination number, CN, to the crystallographic values for the references and to three for the LDH solid samples 1, 5 and 16a. The distances, R, and the Debye–Waller factors, σ^2 , were refined simultaneously. The amplitude reduction factors, S_0^2 , and the shift in threshold energy were varied as a global parameter in the fit procedure. Three different LDH samples were prepared with iodate as shown in Table 9.

Table 9. Synthesis conditions of LDH prepared by coprecipitation from alkaline aqueous solution at 23 °C and pH $\approx 10 - 12$

N	LDH name	M(II)	M(III)	M(II)/M(III)	Anion
LDH 1	$\text{Mg}_3\text{Al-IO}_3$	Mg	Al	3/1	IO_3^-
LDH 5	$\text{Ca}_3\text{Fe-IO}_3$	Ca	Fe	3/1	IO_3^-
LDH 16a	$\text{Mg}_3\text{Al-IO}_3$	Mg	Al	3/1	IO_3^-

Results. The experimental k^3 -weighted spectra of LDH samples 1, 5, 16a and the reference KIO_3 are shown in Fig. 29. The Fourier Transform (FT) of the iodate LDH samples showed a first coordination shell, similar to the KIO_3 reference. This first peak represents the O atoms around iodine. The Fourier transform, FT, of LDH samples 1, 5 and 16a showed a single I–O scattering path at a distance of ca. 1.8 \AA with a fairly low (0.0008\AA^2) Debye–Waller factor, indicating a small bond distance distribution (Table 10). Furthermore, at longer distances there are no contributions to the LDH spectra in comparison with the longer contributions observed in reference KIO_3 measurements. During the fitting procedure, the coordination number of iodine is fixed to three, assuming that iodate is incorporated into LDH and scattering is only present within the IO_3 unit. Additionally, analysis of the EXAFS data showed that the mechanism of iodate incorporation for 1 obtained by coprecipitation and 16a obtained by reconstruction is the same and does not depend on the synthesis route. Sample 5 most probably contains a mixture of calcium and iron(III) iodates and therefore, the contribution from the I–O distance to hydroxo groups in the interlayer space of LDH is not present.

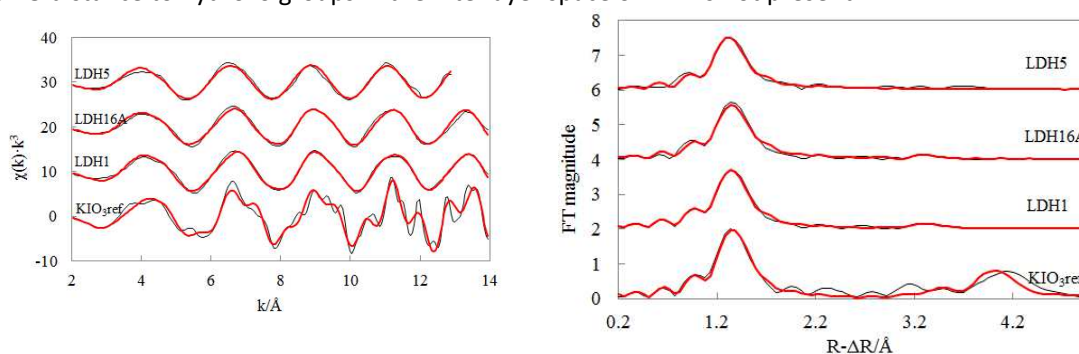


Fig. 29. I K-edge EXAFS of iodate (IO_3^-) sorbed layered double hydroxides and of a potassium iodate reference. Red line – model, black line – experimental.

Table 10. Mean atomic distances, R [\AA], coordination numbers, CN , and Debye-Waller, σ^2 , factors for the iodate containing LDH samples

Sample	Interaction	CN	R , \AA	σ^2
KIO ₃ ref	I – O1	4	1.821±0.024	0.00056
	I – O2	2	2.193±0.139	0.01932
	I···O3	6	4.345±0.062	0.00380
	I···I	6	3.926±0.085	0.00724
LDH 1	I – O1	3	1.812±0.028	0.00078
LDH 5	I – O1	3	1.822±0.028	0.00076
LDH 16a	I – O1	3	1.823±0.031	0.00096

Conclusions. LDH materials, synthesized by coprecipitation, anionic exchange or reconstructions of different compositions, were tested for the capture and immobilization of iodate and iodide from aqueous solutions. The reconstruction method yielded the highest iodate incorporation (ca. 54 % vs. ca. 40 % reached by coprecipitation). It was found that even if the fraction of iodate incorporated into the host structure was relatively high (ca. 40 %), the stability of synthesized iodate-LDH was very low. Heating at 180 C led to nearly 90 % of iodine loss. Additionally, 60 % of incorporated iodate was released after 1 day in brine solution or after 7 days in Milli-Q water. Iodide was incorporated to a lesser extent compared to iodate, probably due to differences in the charge density, size and configuration of the IO₃⁻ and I⁻ ions. EXAFS data showed that, independently of the synthesis route used, the mechanism of iodate incorporation into LDH remains the same. At the present stage of this research we conclude that LDHs can be considered as iodine scavengers for remediation or short-term storage; however, their suitability for long-term storage of radioactive iodine, due to low thermal stability and ease of iodine release in contact with Milli-Q water and brine, should be evaluated in detail considering the specific storage facility. Further investigations of iodine containing LDH properties and stability are required.

This work was performed in collaboration with LUH-IRS (02NUK021G) and has been published (Iglesias et al., 2016).

Further EXAFS results of experiments performed at ROBL, notably on iodide-sorbed apatites and on pertechnetate-sorbed LDH are shown in the final report of LUH (02NUK021G).

2.2 Conclusions

Within this project, we addressed (short-range) structural aspects probed by advanced synchrotron-based EXAFS spectroscopy, and with relevance for the application of monazite-type ceramics as potential nuclear waste forms for separated plutonium, plutonium bearing waste streams and/or minor actinides. The issues include the structural incorporation of lanthanides and actinides into monazite, xenotime and rhabdophane phases, the chemical flexibility of the host phases and phase transition phenomena induced by compositional variations. The results of this work contribute significantly to a refined understanding of the suitability of phosphate-bearing ceramics as potential nuclear waste forms and their long-term stability.

2.2.1 Relevance of results with respect to ceramic waste forms

The work performed within this project focused on single-phase phosphate-based ceramic matrices with monazite, xenotime and rhabdophane structure, respectively, and their potential suitability as

waste forms for specific nuclear waste streams. Major contributions achieved with regard to this question are summarized as follows:

- The incorporation of non-radioactive surrogates for trivalent actinides as well as Cm^{3+} and $\text{Pu}^{3+/4+}$ of up to 15 mol-% Pu within $(\text{La},\text{Pu})\text{PO}_4$ monazite was successfully realized, indicating a structural uptake of plutonium by solid solution formation. In contrast, Ln-phosphates with xenotime structure were found to be unsuitable for the long-term immobilization of trivalent actinides.
- Detailed phase analyses of monazite solid solutions confirmed the formation of regular solid solutions and imply that no preferential incorporation of dopants on host cation sites with similarly sized cationic radii occurs. Furthermore, the flexibility of the monazite structure toward dopants with different cationic radii allows for the co-doping of multiple different actinides and deliberately added inactive elements serving e.g. as neutron poisons to prevent criticality in the nuclear waste forms.
- Extensive structural investigations confirmed the monoclinic structure of rhabdophane – a hydrated low temperature phase of Ln- orthophosphates and a precursor of monazite in wet chemical synthesis routes – and elucidated the phase transition to monazite. Moreover, the formation of single-phase rhabdophane solid solutions was demonstrated. From thermodynamic and dissolution experiments and simulations it was found that rhabdophane is the thermodynamically stable orthophosphate phase below $\sim 80^\circ\text{C}$ which is the expected temperature range in a deep geological repository in the long term. Thus, it can be concluded that in aqueous media a rhabdophane layer will form on the surface of monazite-type waste forms and govern the dissolution behavior under repository conditions.
- A linear correlation between physical properties and lattice parameter of $(\text{La},\text{Eu})\text{PO}_4$ solid solutions was observed allowing for a certain predictability of the investigated parameters in dependence of a chemical composition of pure monazite compounds. These correlations are important input parameter for thermodynamic calculations of monazite waste forms.
- The thermodynamic stability of monazite-type $\text{La}(\text{Eu}/\text{Gd})\text{PO}_4$ solid solutions was demonstrated by a combination of experiments and DFT calculations. Although the solid solutions show excess properties due to strain energy and ion size differences, an immiscibility gap or phase separation of the investigated solid solutions can be excluded. Moreover, these results indicate that the formation of thermodynamically stable solid solutions with monazite structure containing trivalent actinides can be expected. These thermodynamic data provide key output parameters for the calculation of stability and solubility of monazite solid solutions as a function of temperature.

In summary, the work performed within this project yielded in a refined mechanistic understanding of key properties of monazite-type orthophosphate ceramics with respect to their potential application as a nuclear waste forms, in particular for immobilization of actinides.

2.2.2 Knowledge gaps and outlook for future research

Based on the results achieved in this project and considering the outcome of research activities of other groups following knowledge gaps as a basis for future research activities regarding the long-term stability of monazite-type waste forms under repository relevant conditions were identified.

- Generally, more data from experiments on “real” actinide-bearing ceramic waste forms are needed.
- The successful synthesis of Pu containing pyrochlore- and monazite-type solid solutions are very promising and should be extended to design ternary systems considering the incorporation of Gd as a neutron poison material in the waste form. The support of atomistic modelling simulations (simulation of excess properties) will be important to predict the thermodynamic stability of the Pu-bearing binary and ternary solid solutions because calorimetric measurements on these highly radioactive samples are hardly to perform.
- The research into the Ln-phosphate system indicates that rhabdophane will form on the surface of monazite in low-temperature aqueous environments and seems to be the stable

orthophosphate phase in the temperature region that can be expected in a repository in the long-term. For a refined thermodynamic description of the monazite/rhabdophane system under repository conditions more thermodynamic data on rhabdophane solid solutions, e.g. solubility at elevated temperatures and direct measurements of enthalpy of formation are needed.

- Based on previous research we assumed that a rhabdophane layer would form on the surface of the monazite waste form in aqueous environments below 80°C. Therefore, surface-sensitive measurements are needed to prove this assumption in order to verify whether a rhabdophane layer will govern the dissolution behavior of monazite ceramics under repository conditions and in which way this rhabdophane layer will influence the fate of actinides incorporated in monazite waste forms. Complementary experiments with actinides are needed in order to investigate the solubility and dissolution kinetics of “real” waste forms as well as the formation of secondary phases, e.g. Pu³⁺-rhabdophane or Pu⁴⁺-hydroxide).
- As stated by equilibrium thermodynamic calculations the long-term aqueous durability of monazite waste form is very sensitive to the near-field conditions. Dissolution experiments in groundwater-like media are needed to investigate the effect of various ions in the groundwater, e.g. phosphate and fluoride ions on dissolution kinetics and mechanisms under repository conditions.
- A more detailed assessment of the aqueous durability of a phosphate-based ceramic waste form in a cementitious repository require a more complex modelling study incl. reactive transport simulations to understand the effect cementitious material components on the dissolution behavior.
- Concerning the radiation damage effects on monazite and pyrochlore more experimental and simulation studies and especially EXAFS studies are needed to understand the mechanism of amorphization and phase transition, respectively. The investigation of short range ordering effects would allow for a structural description of the damaged phase as well as for a quantification of the damage degree during irradiation. The influence of daughter nuclides, e.g. Pu²⁴¹⁺ → Am²⁴¹ → Np²³⁷ and of the He-built up due to decay events is not completely understood so far.
- A structural description of amorphization and recrystallization of monazite materials is missing so far. Comprehensive investigations on recrystallization kinetics of solid solutions in dependence of chemical composition, temperature and dose rate (dpa as a function of time) are needed in order to understand the correlation of amorphization and recrystallization.
- Very little systematic information is available at present concerning the effect of amorphization on aqueous durability of ceramic waste forms. Dissolution experiments on irradiated samples open up the door to elucidate the influence of structural changes on the aqueous durability of ceramic waste forms.

The experience and knowledge gained in the joint "Conditioning" project forms a promising base for future research activities to solve open question related to a potential application of ceramic materials as nuclear waste forms. The intensive cooperation between the project partners themselves and external groups established a scientific network that offers the scientific infrastructure to address most of the knowledge gaps mentioned above in a follow up "Conditioning II" project. A respective proposal is already under preparation to continue and to strengthen the successful network.

2.2.3 References

- Ankudinov, A.L. and Rehr, J.J. (1997) Relativistic calculations of spin-dependent x-ray-absorption spectra. *Physical Review B* 56, 1712-1728.
- Arinicheva, Y., Bukaemskiy, A., Neumeier, S., Modolo, G. and Bosbach, D. (2014) Studies on thermal and mechanical properties of monazite-type ceramics for the conditioning of minor actinides. *Progress in Nuclear Energy* 72, 144-148.

Arinicheva, Y., Popa, K., Scheinost, A.C., Rossberg, A., Dieste-Blanco, O., Raison, P., Cambriani, A., Neumeier, S., Somers, J., Dirk and Bosbach (submitted) Structural investigations of (La,Pu)PO₄ monazite solid solutions: XRD and XAFS study. *Journal of Nuclear Materials*.

Bamberger, C.E., Begun, G.M. and Haire, R.G. (1984) Synthesis and Characterization of Actinide Phosphates. *Inorganica Chimica Acta* 94, 41-41.

Belin, R.C., Martin, P.M., Valenza, P.J. and Scheinost, A.C. (2009) Experimental insight into the radiation resistance of zirconia-based americium ceramics. *Inorg. Chem.* 48, 5376-5381.

Bjorklund, C.W. (1957) THE PREPARATION OF PUP₂O₇ AND PUPO₄. *Journal of the American Chemical Society* 79, 6347-6350.

Boakye, E.E., Hay, R.S., Mogilevsky, P. and Cinibulk, M.K. (2008) Two phase monazite/xenotime 30LaPO₄(4)-70YPO₄(4) coating of ceramic fiber tows. *Journal of the American Ceramic Society* 91, 17-25.

Bouty, O., Ramond, L., Solari, P.L. and Cammelli, S. (2016) XANES analysis of a Cm-doped borosilicate glass under alpha-self-irradiation effects. *Journal of Materials Science* 51, 7918-7928.

Bregiroux, D., Belin, R., Valenza, P., Audubert, F. and Bernache-Assollant, D. (2007) Plutonium and americium monazite materials: Solid state synthesis and X-ray diffraction study. *Journal of Nuclear Materials* 366, 52-57.

Bregiroux, D., Lucas, S., Champion, E., Audubert, F. and Bernache-Assollant, D. (2006) Sintering and microstructure of rare earth phosphate ceramics REPO₄ with RE = La, Ce or Y. *Journal of the European Ceramic Society* 26, 279-287.

Burakov, B.E., Yagovkina, M.A., Garbuzov, V.M., Kitsay, A.A. and Zirlin, V.A. (2004) Self-irradiation of monazite ceramics: Contrasting behavior of PuPO₄ and (La,Pu)PO₄ doped with Pu-238, in: Hanchar, J.M., StroesGascoyne, S., Browning, L. (Eds.), *Scientific Basis for Nuclear Waste Management Xviii*, pp. 219-224.

Clavier, N., Szenknect, S., Costin, D.T., Mesbah, A., Poinssot, C. and Dacheux, N. (2014) From thorite to coffinite: A spectroscopic study of Th_{1-x}U_xSiO₄ solid solutions. *Spectrochimica Acta Part a-Molecular and Biomolecular Spectroscopy* 118, 302-307.

de Kerdaniel, E.D., Clavier, N., Dacheux, N., Terra, O. and Podor, R. (2007) Actinide solubility-controlling phases during the dissolution of phosphate ceramics. *Journal of Nuclear Materials* 362, 451-458.

Deschanel, X., Picot, V., Glorieux, B., Jorion, F., Peugeot, S., Roudil, D., Jegou, C., Broudic, V., Cachia, J.N., Advocat, T., Den Auwer, C., Fillet, C., Coutures, J.P., Hennig, C. and Scheinost, A. (2006) Plutonium incorporation in phosphate and titanate ceramics for minor actinide containment. *J. Nucl. Mater.* 352, 233-240.

Ellis, D.E., Terra, J., Warschkow, O., Jiang, M., Gonzalez, G.B., Okasinski, J.S., Bedzyk, M.J., Rossi, A.M. and Eon, J.G. (2006) A theoretical and experimental study of lead substitution in calcium hydroxyapatite. *Physical Chemistry Chemical Physics* 8, 967-976.

Funke, H., Scheinost, A.C. and Chukalina, M. (2005) Wavelet analysis of extended X-ray absorption fine structure data. *Physical Review B* 71, 094110.

Hazemann, J.L., Manceau, A., Sainctavit, P. and Malgrange, C. (1992) STRUCTURE OF THE ALPHA-FEXAL1-XOOH SOLID-SOLUTION .1. EVIDENCE BY POLARIZED EXAFS FOR AN EPITAXIAL-GROWTH OF HEMATITE-LIKE CLUSTERS IN FE-DIASPORE. *Physics and Chemistry of Minerals* 19, 25-38.

Henderson, C.M.B., Redfern, S.A.T., Smith, R.I., Knight, K.S. and Charnock, J.M. (2001) Composition and temperature dependence of cation ordering in Ni-Mg olivine solid solutions: a time-of-flight neutron powder diffraction and EXAFS study. *American Mineralogist* 86, 1170-1187.

Hennig, C., Skanthakumar, S. and Soderholm, L. (2010) Double photoexcitation of 2p and 4f electrons in curium. *J Electron Spectrosc* 180, 17-20.

Hobart, D.E., Begun, G.M., Haire, R.G. and Hellwege, H.E. (1983) RAMAN-SPECTRA OF THE TRANSPLUTONIUM ORTHO-PHOSPHATES AND TRIMETAPHOSPHATES. *Journal of Raman Spectroscopy* 14, 59-62.

Huittinen, N., Scheinost, A.C., Wilden, A., Arinicheva, Y. and Stumpf, T. (in preparation) A spectroscopic study on Cm³⁺ incorporation in lanthanide phosphate rhabdophane (LnPO₄·nH₂O) and monazite (LnPO₄).

Iglesias, L., Walther, C., Medina, F., Holzer, A., Neumann, A., Lozano-Rodriguez, M.J., Alvarez, M.G. and Torapava, N. (2016) A comprehensive study on iodine uptake by selected LDH phases via coprecipitation, anionic exchange and reconstruction. *J. Radioanal. Nucl. Chem.* 307, 111-121.

Jardin, R., Pavel, C.C., Raison, P.E., Bouexiere, D., Santa-Cruz, H., Konings, R.J.M. and Popa, K. (2008) The high-temperature behaviour of PuPO₄ monazite and some other related compounds. *Journal of Nuclear Materials* 378, 167-171.

Keller, C. and Walter, K.H. (1965) DARSTELLUNG GITTERKONSTANTEN UND CHEMISCHE EIGENSCHAFTEN EINIGER TERNARER OXIDE DES PLUTONIUMS AMERICIUMS UND CURIUMS VOM TYP ME₃XO₄. *Journal of Inorganic & Nuclear Chemistry* 27, 1253-&.

Kowalski, P.M., Ji, Y., Li, Y., Arinicheva, Y., Beridze, G., Neumeier, S., Bukaemskiy, A. and Bosbach, D. (2017) Simulation of ceramic materials relevant for nuclear waste management: Case of La_{1-x}Eu_xPO₄ solid solution. *Nuclear Instruments and Methods in Physics Research B* 393, 68-72.

Martin, P., Grandjean, S., Valot, C., Carlot, G., Ripert, M., Blanc, P. and Hennig, C. (2007) XAS study of (U_{1-y}Pu_y)O₂ solid solutions. *J Alloy Compd* 444, 410-414.

Martin, P.M., Belin, R.C., Valenza, P.J. and Scheinost, A.C. (2009) EXAFS study of the structural phase transition in the americium zirconate pyrochlore. *J. Nucl. Mater.* 385, 126–130.

Martins, J.L. and Zunger, A. (1984) Bond lengths around isovalent impurities and in semiconductor solid-solutions. *Physical Review B* 30, 6217-6220.

Mesbah, A., Clavier, N., Elkaim, E., Gausse, C., Ben Kacem, I., Szenknect, S. and Dacheux, N. (2014) Monoclinic form of the rhabdophane compounds: REEPO₄ · 0.667H₂O. *Crystal Growth & Design* 14, 5090-5098.

Mesbah, A., Clavier, N., Lozano-Rodriguez, J., Szenknect, S. and Dacheux, N. (2016) Incorporation of thorium in the zircon structure type through the Th_{1-x}Er_x(SiO₄)_{1-x}(PO₄)_x thorite-xenotime solid solution. *Inorg. Chem.* 55, 11273–11282.

Mooney, R.C.L. (1948) Crystal structures of a series of rare earth phosphates. *Journal of Chemical Physics* 16, 1003-1003.

Mooney, R.C.L. (1950) X-ray diffraction study of cerous phosphate and related crystals. 1. Hexagonal modification. *Acta Crystallographica* 3, 337-340.

Nastren, C., Jardin, R., Somers, J., Walter, M. and Brendebach, B. (2009) Actinide incorporation in a zirconia based pyrochlore (Nd(1.8)An(0.2))Zr₂O_{7+x} (An = Th, U, Np, Pu, Am). *Journal of Solid State Chemistry* 182, 1-7.

Ni, Y.X., Hughes, J.M. and Mariano, A.N. (1995) Crystal chemistry of the monazite and xenotime structures. *American Mineralogist* 80, 21-26.

Oelkers, E.H. and Poitrasson, F. (2002) An experimental study of the dissolution stoichiometry and rates of a natural monazite as a function of temperature from 50 to 230 degrees C and pH from 1.5 to 10. *Chemical Geology* 191, 73-87.

Poitrasson, F., Oelkers, E., Schott, J. and Montel, J.M. (2004) Experimental determination of synthetic NdPO₄ monazite end-member solubility in water from 21 degrees C to 300 degrees C: Implications for rare earth element mobility in crustal fluids. *Geochimica Et Cosmochimica Acta* 68, 2207-2221.

Popa, K., Colineau, E., Wastin, F. and Konings, R.J.M. (2007) The low-temperature heat capacity of (Pu_{0.1}La_{0.9})PO₄. *Solid State Communications* 144, 74-77.

Popa, K., Raison, P.E., Martel, L., M.Martin, P., DamienPrieur, L.Solari, P., DanielBouëxière, J.M.Konings, R. and JosephSomers (2016) StructuralinvestigationsofPuIII phosphatebyX-raydiffraction,MAS-NMR andXANESspectroscopy. *Journal of Solid State Chemistry* 230, 169-174.

Rafiuddin, M.R. and Grosvenor, A.P. (2016) A Structural Investigation of Hydrated and Anhydrous Rare-Earth Phosphates. *Inorganic Chemistry* 55, 9685-9695.

- Rai, D., Felmy, A.R. and Fulton, R.W. (1992) SOLUBILITY AND ION ACTIVITY PRODUCT OF AMPO4.XH2O(AM). *Radiochimica Acta* 56, 7-14.
- Ravel, B. and Newville, M. (2005) ATHENA, ARTEMIS, HEPHAESTUS: data analysis for X-ray absorption spectroscopy using IFEFFIT. *Journal of Synchrotron Radiation* 12, 537-541.
- Ressler, T. (1998) WinXAS: a Program for X-ray Absorption Spectroscopy Data Analysis under MS-Windows. *Journal of Synchrotron Radiation* 5, 118-122.
- Rosberg, A., Reich, T. and Bernhard, G. (2003) Complexation of uranium(VI) with protocatechuic acid - application of iterative transformation factor analysis to EXAFS spectroscopy. *Anal. Bioanal. Chem.* 376, 631-638.
- Scavini, M., Coduri, M., Allietta, M., Brune, M. and Ferrero, C. (2012) Probing Complex Disorder in Ce_{1-x}Gd_xO_{2-x/2} Using the Pair Distribution Function Analysis. *Chem. Mat.* 24, 1338-1345.
- Scheinost, A.C., Schulze, D.G. and Schwertmann, U. (1999) Diffuse reflectance spectra of Al substituted goethite: A ligand field approach. *Clays and Clay Minerals* 47, 156-164.
- Scheinost, A.C., Stanjek, H., Schulze, D.G., Gasser, U. and Sparks, D.L. (2001) Structural environment and oxidation state of Mn in goethite-groutite solid-solutions. *American Mineralogist* 86, 139-146.
- Shannon, R.D. and Prewitt, C.T. (1969) Effective ionic radii in oxides and fluorides. *Acta Crystallographica Section B-Structural Crystallography and Crystal Chemistry B* 25, 925-946.
- Taylor, M. and Ewing, R.C. (1978) Crystal structures of ThSiO₄ polymorphs - huttonite and thorite. *Acta Crystallographica Section B - Structural Science* 34, 1074-1079.
- Vantelon, D., Montarges-Pelletier, E., Michot, L.J., Briois, V., Pelletier, M. and Thomas, F. (2003) Iron distribution in the octahedral sheet of dioctahedral smectites. An FeK-edge X-ray absorption spectroscopy study. *Physics and Chemistry of Minerals* 30, 44-53.
- Walter, M., Somers, J., Bouexiere, D. and Rothe, J. (2011) Local structure in solid solutions of stabilised zirconia with actinide dioxides (UO₂, NpO₂). *Journal of Solid State Chemistry* 184, 911-914.
- Zhang, Y.J. and Vance, E.R. (2008) Plutonium in monazite and brabantite: Diffuse reflectance spectroscopy study. *Journal of Nuclear Materials* 375, 311-314.

2.3 Fortschritt auf dem Gebiet des Vorhabens anderer Stellen

Da an der Thematik zu innovativen Abfallformen ein reges internationales Interesse besteht, befassen sich andere Forschungsgruppen ebenfalls mit der Untersuchung von keramischen Abfallformen. Komplementäre endlagerrelevante Studien werden insbesondere

- am Institut de Chimie Séparative de Marcoule (ICSM), Marcoule, Frankreich,
- am Department of Materials Science and Engineering der University of Sheffield in Großbritannien,
- am Department of Geological and Environmental Sciences, Stanford University, USA und der
- Australian Nuclear Science and Technology Organisation (ANSTO), Sydney, Australien

durchgeführt. Das Institut für Ressourcenökologie mit der institutseigenen Rossendorf Beamline an der ESRF pflegt intensive Kooperationen zu den internationalen Forschungsinstituten.

Die aktuellen Forschungsaktivitäten befassen sich mit der Synthese [Yan2009], [Zeng2014], [Schildhammer2016], Struktur [Mesbah2014], [Popa2016], sowie der Langzeitstabilität [Deschanel2014], [Raffiudin2015], [Ma2015] und thermodynamischen Eigenschaften [Gausse2016], [Gavrichev2016].

Deschanel, X., Seydoux-Guillaume, A., Magnin, V., Mesbah, A., Tribet, M., Moloney, M., Serruys, Y., Peugeot, S. 2014. Swelling induced by alpha decay in monazite and zirconolite ceramics: A XRD and TEM comparative study. *Journal of Nuclear Materials* 448(1-3): 184–194.

Gausse, C., Szenknect, S., Qin, D.W., Mesbah, A., Clavier, N., Neumeier, S., Bosbach, D., Dacheux, N. 2016. Determination of the solubility of rhabdophane LnPO₄·0.667H₂O (Ln = La to Dy). *European Journal of Inorganic Chemistry*, 28: 4615-4630.

- Gavrichev, K., Gurevich, V., Ryumin, M., Tyrin, A., Komissarova, L. 2016. Low-temperature heat capacity and thermodynamic properties of PrPO_4 . *Geochemistry International* 54: 362–368.
- Ma, J., Teng, Y., Huang, Y., Wu, L., Zhang, K., Zhao X. 2015. Effects of sintering process, pH and temperature on chemical durability of $\text{Ce}_{0.5}\text{Pr}_{0.5}\text{PO}_4$ ceramics. *Journal of Nuclear Materials* 465: 550–555.
- Mesbah, A., Clavier, N., Elkaim, E., Gausse, C., Kacem, I.B., Szenknect, S., Dacheux, N. 2014: Monoclinic form of the rhabdophane compounds: $\text{REEPO}_4 \cdot 0.667\text{H}_2\text{O}$. *Crystal Growth and Design* 14(10): 5090–5098.
- Popa, K., Raison, P.E., Martel, L., Martin, P.M., Prieur, D., Solari, P.L., Bouëxière, D., Konings, R.J.M., Somers, J. 2015. Structural investigations of Pu^{III} phosphate by X-ray diffraction, MAS-NMR and XANES spectroscopy. *Journal of Solid State Chemistry* 230: 169 – 174.
- Rafiuddin, M.R., Grosvenor, A.P. 2015. Probing the effect of radiation damage on the structure of rare-earth phosphates. *Journal of Alloys and compounds* 653: 279–289.
- Schildhammer, D., Petschnig, L.L., Fuhrmann, G., Heymann, G., Tribus, M., Schottenberger, H., Huppertz, H. 2016. Synthesis and characterization of the novel rare earth orthophosphates $\text{Y}_{0.5}\text{Er}_{0.5}\text{PO}_4$ and $\text{Y}_{0.5}\text{Yb}_{0.5}\text{PO}_4$. *Zeitschrift für Naturforschung B* 71: 65–70.
- Weber, W.J., Navrotsky, A., Stefanovsky, S., Vance, E.R., Vernaz, E. 2009. Materials science of high-level nuclear waste immobilization. *MRS Bulletin* 34: 46–53.
- Yang, P., Quan, Z., Li, C. Hou, Z. Wang, W., Lin, J. 2009. Solvothermal synthesis and luminescent properties of monodisperse $\text{LaPO}_4:\text{Ln}$ ($\text{Ln}=\text{Eu}^{3+}$, Ce^{3+} , Tb^{3+}) particles. *Journal of Solid State Chemistry* 182: 1045–1054.
- Zeng, P., Teng, Y., Huang, Y., Wu, L., Wang, X., 2014. Synthesis, phase structure and microstructure of monazite-type $\text{Ce}_{1-x}\text{Pr}_x\text{PO}_4$ solid solutions for immobilization of minor actinide neptunium. *Journal of Nuclear Materials* 452: 407–413.

2.4 Publikationen der Ergebnisse

2.4.1 Begutachtete Artikel in wissenschaftlichen Zeitschriften

Mesbah, A., Szenknect, S., Clavier, N., Lozano-Rodriguez, J., Poinssot, C., Auwer, C.D., Ewing, R.C. and Dacheux, N. (2015) Coffinite, USiO_4 , is abundant in nature: So why is it so difficult to synthesize? *Inorg. Chem.* 54, 6687–6696.

Iglesias, L., Walther, C., Medina, F., Holzer, A., Neumann, A., Lozano-Rodriguez, M.J., Alvarez, M.G. and Torapava, N. (2016) A comprehensive study on iodine uptake by selected LDH phases via coprecipitation, anionic exchange and reconstruction. *Journal of Radioanalytical and Nuclear Chemistry* 307, 111–121.

Mesbah, A., Clavier, N., Lozano-Rodriguez, J., Szenknect, S. and Dacheux, N. (2016) Incorporation of thorium in the zircon structure type through the $\text{Th}_{1-x}\text{Er}_x(\text{SiO}_4)_{1-x}(\text{PO}_4)_x$ thorite-xenotime solid solution. *Inorganic Chemistry* 55, 11273–11282.

Arinicheva, Y., Popa, K., Scheinost, A.C., Rossberg, A., Dieste-Blanco, O., Raison, P., Cambriani, A., Neumeier, S., Somers, J., Dirk and Bosbach (submitted) Structural investigations of $(\text{La,Pu})\text{PO}_4$ monazite solid solutions: XRD and XAFS study. *Journal of Nuclear Materials*.

Huittinen, N., Scheinost, A.C., Wilden, A., Arinicheva, Y. and Stumpf, T. (in preparation) A spectroscopic study on Cm^{3+} incorporation in lanthanide phosphate rhabdophane ($\text{LnPO}_4 \cdot n\text{H}_2\text{O}$) and monazite (LnPO_4).

2.4.2 Vorträge auf nationalen und internationalen Konferenzen

J.M. Lozano-Rodriguez, Y. Arinicheva, S. Neumeier, A.C. Scheinost: Monazite as promising candidates for nuclear waste management: Structural characterization by X-ray absorption spectroscopy. Actinide XAS, Bottstein, Switzerland, **2014**.

S. Neumeier, P.K. Kulriya, Y. Arinicheva, N. Huittinen, J. Lozano-Rodriguez, G. Deissmann, D. Bosbach.: Structural *in-situ* investigations on (La,Eu)PO₄ and (La,Gd)PO₄ solid solution series under heavy ion irradiation. 57th Accelerator User Workshop, Delhi, India. **2014 (invited)**.

M.J. Lozano-Rodriguez, Y. Arinicheva, J. Heuser, K. Kvashnina, S. Neumeier, A.C. Scheinost: Determination of local structure in mixed lanthanoid phosphate solid solutions by X-ray absorption spectroscopy. E-MRS, Lille, France, **2015**.

M.J. Lozano-Rodriguez, Y., Arinicheva, J. Holthausen, S. Neumeier, A.C. Scheinost: Structural stability study of the mixed La_{0.7-x}Lu_xEu_{0.3}PO₄ solid solutions by Extended X-ray Absorption Spectroscopy. MRS - Scientific Basis for Nuclear Waste Management XXXIX, Montpellier, France, **2015 (invited)**.

S. Neumeier, Y. Arinicheva, N. Huittinen, M.J. Lozano-Rodriguez, J. Holthausen, G. Modolo, A.C. Scheinost, T. Stumpf, D. Bosbach: Spectroscopic studies on monazite-type ceramics for the conditioning of radioactive waste: Infrared, Raman, X-ray Absorption and Site-Selective Time Resolved Laser Fluorescence Spectroscopy. E-MRS, Lille, France, **2015 (invited)**.

2.4.3 Poster auf nationalen und internationalen Konferenzen

Y. Arinicheva, M.J. Lozano-Rodriguez, S. Neumeier, A.C. Scheinost, N. Clavier, D. Bosbach: Structural studies on (La,Eu)PO₄ solid solutions by Infrared, Raman and X-ray Absorption Spectroscopy. Advanced Techniques in Actinide Spectroscopy (ATAS), Dresden, Germany, **2014**.

Y. Arinicheva, M.J. Lozano-Rodrigues, A.C. Scheinost, N. Clavier, N. Dacheux, D. Bosbach, S. Neumeier: Structural studies on (La,Eu)PO₄ solid solutions by Infrared, Raman and X-ray Absorption Spectroscopy. 25th Seminar on Activation Analysis and Gamma Spectroscopy (SAAGAS), Aachen, Germany, **2015**.

N. Huittinen, A. Scheinost, A. Wilden, Y. Arinicheva: Cm³⁺ incorporation in La_{1-x}Gd_xPO₄ monazites: a TRLS and XAS study. 9th International Conference on Nuclear and Radiochemistry (NRC9), Helsinki, Finland, **2016**.

Berichtsblatt

1. ISBN oder ISSN	2. Berichtsart (Schlussbericht oder Veröffentlichung) Schlussbericht
3. Titel Fachlicher Schlussbericht des BMBF Forschungsvorhabens „Verbundprojekt: Grundlegende Untersuchungen zur Immobilisierung langlebiger Radionuklide mittels Einbau in endlagerrelevante Keramiken (Conditioning) – Teilprojekt B“	
4. Autor(en) [Name(n), Vorname(n)] Scheinost, Andreas Lozano-Rodriguez, Janeth	5. Abschlussdatum des Vorhabens 30. Juni 2016
	6. Veröffentlichungsdatum 31.03.2017
	7. Form der Publikation Schlussbericht
8. Durchführende Institution(en) (Name, Adresse) Helmholtz-Zentrum Dresden-Rossendorf Institut für Ressourcenökologie Bautzner Landstr. 400 01328 Dresden	9. Ber. Nr. Durchführende Institution
	10. Förderkennzeichen 02NUK021B
	11. Seitenzahl 45
12. Fördernde Institution (Name, Adresse) Bundesministerium für Bildung und Forschung (BMBF) 53170 Bonn	13. Literaturangaben 51
	14. Tabellen 10
	15. Abbildungen 29
16. Zusätzliche Angaben	
17. Vorgelegt bei (Titel, Ort, Datum)	
18. Kurzfassung In dem Teilprojekt 02NUK021B wurde mit Hilfe von Synchrotron-EXAFS-Spektroskopie der Mechanismus des Einbaus der dreiwertigen Lanthanoide La, Sm, Eu, Tb und Lu, sowie der dreiwertigen Aktinoide Pu und Cm in Monazit- und Xenotim-Keramiken sowie in dem Verwitterungsprodukt Rhabdophan untersucht. Aufgrund der spektroskopischen Ergebnisse lassen sich folgende Schlussfolgerungen ziehen: <ul style="list-style-type: none"> • Monazite können einen relativ hohen Prozentsatz kleinerer dreiwertiger Ionen (Lu, Pu, Cm) einbauen, indem diese die Kationenpositionen im Kristallgitter von Monazit einnehmen. • Die Größe der Einheitszelle nimmt mit zunehmendem Einbau linear entsprechend der Vegard-Regel ab, ohne dass ein Übergang in die Struktur von Xenotim stattfindet. • Diese strukturelle Flexibilität wird dadurch erreicht, dass sich die längere und daher schwächere La-O Bindung mit zunehmendem Einbau verkürzt und an die Bindungslängen der kleineren Kationen anpasst. Die Sauerstoff-Bindungslängen der kleineren Kationen bleiben dagegen fast unverändert. • Rhabdophan kann ebenso wie Monazit kleinere Kationen durch strukturelle Substitution einbauen. EXAFS bestätigte die kürzlich gefundene monokline Struktur mit einer Mischung aus 8-fach und 9-fach koordinierten Kationen. Basierend auf diesen Ergebnissen kann die Monazit-Keramik als gute Gastphase für die Inkorporation von dreiwertigen Lanthanoiden und Aktinoiden angesehen werden. Selbst bei einer über lange Zeiträume möglichen oberflächlichen Verwitterung einhergehend mit Rhabdophanbildung sollten die eingeschlossenen Fremdkationen inkorporiert bleiben. Dagegen muss von einer Verwendung der Xenotim-Keramiken als Entsorgungsform abgesehen werden, da der Einbau relevanter dreiwertiger Radionuklide langfristig nur in geringem Umfang stattfindet.	
19. Schlagwörter EXAFS, Monazit, Xenotim, Rhabdophan, Pu ³⁺ , Cm ³⁺ , Minore Aktinoide, Solid-Solution, Einbau, Immobilisierung	
20. Verlag	21. Preis

Document Control Sheet

1. ISBN or ISSN	2. type of document (e.g. report, publication) Final Report
3. title Fachlicher Schlussbericht des BMBF Forschungsvorhabens „Verbundprojekt: Grundlegende Untersuchungen zur Immobilisierung langlebiger Radionuklide mittels Einbau in endlagerrelevante Keramiken (Conditioning) – Teilprojekt B“	
4. author(s) (family name, first name(s)) Scheinost, Andreas Lozano-Rodriguez, Janeth	5. end of project June 30, 2016
	6. publication date March 31, 2017
	7. form of publication Final Report
8. performing organization(s) (name, address)	9. originator's report no.
	10. reference no. 02NUK021B
	11. no. of pages 45
12. sponsoring agency (name, address) Bundesministerium für Umwelt, Naturschutz und Reaktorsicherheit (BMU) Alexanderstraße 3 10178 Berlin	13. no. of references 51
	14. no. of tables 10
	15. no. of figures 29
16. supplementary notes	
17. presented at (title, place, date)	
18. abstract Within the project 02NUK021B, we investigated with synchrotron EXAFS spectroscopy the mechanisms of incorporation for the trivalent lanthanoids La, Sm, Eu, Tb and Lu, as well as for the trivalent actinoids Pu and Cm, by monazite and xenotime ceramics and the weathering product rhabdophane. Based on the spectroscopic results, we conclude that: <ul style="list-style-type: none"> • Monazite ceramics are able to host a relatively high percentage of smaller (compared to La³⁺) trivalent cations (Lu, Pu, Cm) by structural incorporation; the cations reside in the regular crystallographic lattice positions of monazite. • The size of the unit cell decreases linearly with increasing substitution according to Vegard's law; without the structural transition to xenotime taking place. • This structural flexibility is realized through an adaptive shortening of the longer and hence weaker La-O bonds with increasing substitution, while the corresponding bond lengths of the smaller cations are hardly changing. • Likewise to monazite, rhabdophane is able to incorporate smaller cations by structural substitution. By EXAFS, we could confirm the recently found monoclinic structure with a mixture of 8- and 9-coordinated cations. Based on our results, monazite ceramics seem to be well suited for hosting trivalent lanthanoids and actinoids with relevance for nuclear waste disposal. Even under long-term weathering, which may convert the surface layers of monazite into rhabdophane, the small trivalent cations will be hosted by rhabdophane as well, and hence should not be released. In contrast, xenotime should not be considered as waste disposal form, since substitution of different-sized trivalent cations is on the long term marginal.	
19. keywords EXAFS, monazite, xenotime, rhabdophane, Pu ³⁺ , Cm ³⁺ , minor actinoids, solid-solution, incorporation, immobilization	
20. publisher	21. price